lajss.org
Latin American Journal of Solids and Structures
www.lajss.org

A smoothed DSG4 flat-shell framework for dynamic analysis of auxetic honeycomb sandwich shells with elastic boundary conditions

Le Hong Hieu[1], Quoc Hoa Pham[2], Nhan Thinh Hoang[3,*]

[1] HUTECH Institute of Engineering, HUTECH University, Ho Chi Minh City, Vietnam. Email: lh.hieu@hutech.edu.vn
[2] Faculty of Mechanical Engineering, Tran Dai Nghia University, Ho Chi Minh City, Vietnam. Email: quochoavhp@gmail.com
[3] Institute of International Education, Nguyen Tat Thanh University, Ho Chi Minh City, Vietnam. Email: htnhan@ntt.edu.vn

* Corresponding author. Email: htnhan@ntt.edu.vn

Abstract

This study develops a novel smoothed discrete shear gap four-node (SM-DSG4) flat-shell element for free-vibration and transient analyses of auxetic honeycomb sandwich shells with elastic boundary conditions. The methodological novelty lies in introducing cell-based smoothing into the DSG4 membrane and bending strain fields while preserving discrete shear gap interpolation for transverse shear, without adding nodal degrees of freedom. The re-entrant honeycomb core is represented by an equivalent orthotropic continuum, and distributed translational and rotational springs model finite boundary restraint. Comparisons with published benchmarks yield relative errors below 2% for the investigated auxetic honeycomb sandwich panels. Relative to conventional DSG4, SM-DSG4 reduces distortion-induced fundamental-frequency drift by approximately 6.4–10.3% for the examined meshes at a distortion level of 0.3. Parametric results demonstrate that shell curvature and re-entrant cell angle affect natural frequencies, whereas increasing support stiffness raises frequencies toward the corresponding constrained limits and reduces transient response amplitudes in the examined cases. The proposed formulation provides a numerical tool for evaluating the combined effects of auxetic core geometry and realistic boundary flexibility on sandwich-shell dynamics.

Keywords

Honeycomb sandwich shell; SM-DSG4 element; Elastic boundary condition; Blast-type loading; Transient response; Free vibration

1 INTRODUCTION

Shell structures are extensively employed in aerospace, marine, transportation, energy and protective systems because their curved geometry provides high load-carrying efficiency at relatively low structural weight. Their mechanical response, however, is strongly coupled with curvature, thickness, material constitution, support conditions and loading characteristics. Consequently, reliable prediction of natural frequencies and transient responses remains an active topic in computational mechanics. Recent studies have addressed free vibration of functionally graded porous shells in thermal environments (Abuteir and Boutagouga, 2022), vibration of composite cylindrical shells using finite element and analytical approaches (Farazin et al., 2022), and meshless analysis of bulkhead-stiffened functionally graded open shells (Kwak et al., 2022). Other investigations have considered graphene-reinforced porous cylindrical panels (Cho, 2023), spectral finite element models for functionally graded shells with nonuniform thickness (Valencia Murillo et al., 2023), blast-pressure distributions on cylindrical shells (Yin et al., 2023), and three-dimensional finite element modeling of the free vibration of functionally graded sandwich plates (Burlayenko and Sadowski, 2020). These contributions demonstrate that shell behavior is particularly sensitive to geometric curvature, material architecture and boundary conditions, especially when lightweight constructions are subjected to dynamic or short-duration loads.

Among lightweight sandwich configurations, honeycomb cores are attractive because they combine low density with high specific stiffness, favorable energy absorption and efficient load transfer between the face sheets. For shell structures, replacing the discrete cellular core by an equivalent orthotropic continuum is especially useful because it avoids explicit cell-level discretization while retaining the main stiffness characteristics of the core. Li et al. (2020) combined experiments and shell theory to study the free flexural vibration of thin-walled honeycomb sandwich cylindrical shells and demonstrated the usefulness of an equivalent orthotropic representation. The role of auxetic

honeycomb geometry has subsequently received increasing attention. Li and Liu (2022) investigated thermal buckling and free vibration of viscoelastic functionally graded sandwich shells with a tunable auxetic core, while Pham et al. (2022) examined free vibration and optimization of doubly curved stiffened sandwich shells with functionally graded skins and an auxetic honeycomb layer. Analytical modeling has also been extended to fiber-reinforced composite honeycomb cylindrical-spherical combined shells (Li et al., 2022). These studies consistently show that cell geometry and the associated effective orthotropic properties can substantially modify the stiffness and vibration characteristics of sandwich shells.

The advantages of auxetic and honeycomb cores are also important under impact and blast-type loading. Bohara et al. (2022) proposed a dual-mechanism auxetic-core protective sandwich concept and reported improved energy absorption and reduced stress transmission. Razgordanisharahi et al. (2023) analyzed the free vibration of cylindrical honeycomb sandwich panels using a state-space Levy method, emphasizing the influence of honeycomb geometry and support conditions. Impact analyses of stiffened doubly curved shells with re-entrant auxetic cores have further confirmed the sensitivity of the structural response to the core configuration (Fu et al., 2023), whereas blast investigations of honeycomb sandwich structures with hybrid face sheets have highlighted the benefits of the cellular core for reducing deformation and increasing specific energy absorption (Patel et al., 2023). Bio-inspired sandwich cores have likewise been proposed for high-strain-rate energy absorption (Ghanbari and Panirani, 2024). More recent work has considered honeycomb cylindrical shells with graphene-based coatings (Thang et al., 2025). Collectively, these works confirm the potential of honeycomb and auxetic cores for vibration control and dynamic protection, but they also show that the response is governed by several interacting parameters rather than by the core topology alone.

Recent advances in micro-/nanostructured materials have emphasized the importance of generalized continuum theories in capturing size-dependent mechanical behavior (Faghidian et al., 2022; Faghidian and Elishakoff, 2023; Faghidian and Darban, 2024; Challamel et al., 2025). Meanwhile, developments in mechanical metamaterials have highlighted the roles of cellular architecture and homogenization in predicting effective structural properties (Li et al., 2023; Siniauskaya et al., 2024). These studies provide complementary perspectives on multiscale mechanics, whereas the present work focuses on the numerical formulation of homogenized auxetic sandwich shells.

The accurate numerical analysis of auxetic honeycomb sandwich shells remains challenging when conventional low-order shell elements are employed. In particular, these elements may suffer from transverse shear locking, membrane locking, and sensitivity to mesh distortion, especially in thin-shell applications. Recent computational developments have also introduced a four-node mixed flat-shell element for variable-stiffness composite laminates (Liguori et al., 2024), refined higher-order formulations for laminated anisotropic doubly curved shells of arbitrary shape (Tornabene et al., 2026), and a spring-based Ritz approach for shell vibrations under arbitrary boundary conditions (Shi et al., 2016). Strain-smoothing techniques have therefore been developed to improve the behavior of standard finite elements without introducing high-order interpolation. Nguyen-Thanh et al. (2008) proposed a smoothed finite element method for shell analysis, and Cui et al. (2010) developed an edge-based smoothed formulation for plates and shells. Cell-based smoothing was subsequently applied to shell free-vibration and buckling problems (Thai-Hoang et al., 2011). In parallel, the discrete shear gap (DSG) concept has proved effective for suppressing parasitic transverse shear modes. Nguyen-Xuan et al. (2010) combined strain smoothing with a stabilized DSG technique for Reissner-Mindlin plates, while Nguyen-Thoi et al. (2013) extended the smoothed DSG concept to shell structures using triangular elements. Related developments include edge-based smoothed MITC shell elements for laminated composites (Pham et al., 2018) and strain-smoothed MITC3+ shell elements (Lee and Lee, 2019). More recently, Chen et al. (2022) combined strain smoothing with the DSG concept in a triangular Reissner-Mindlin flat-shell formulation, confirming the effectiveness of treating membrane-bending and transverse-shear fields separately. These studies provide a strong numerical foundation for robust low-order shell elements, but their applications have mainly concerned homogeneous, laminated, or conventional composite shell benchmarks.

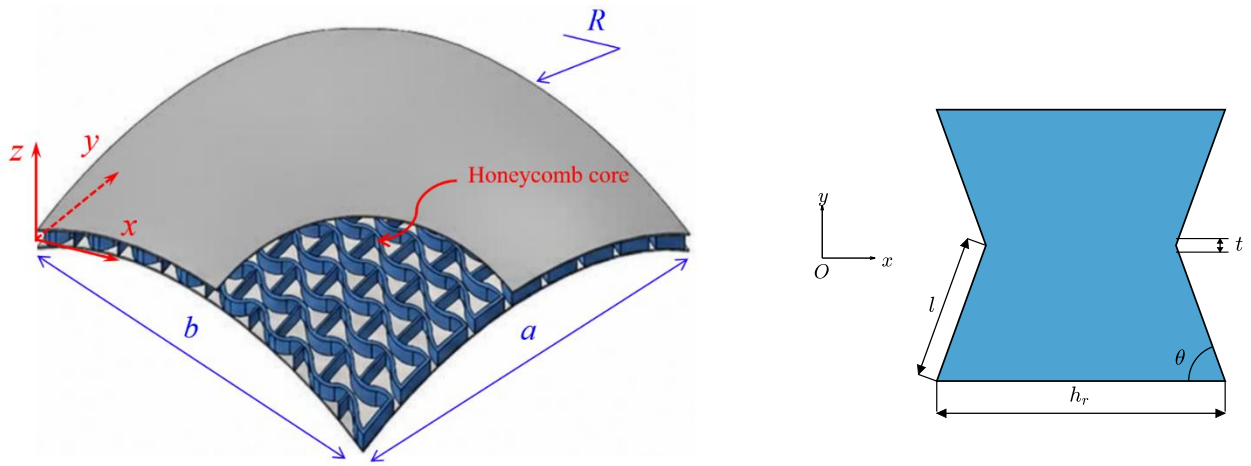
Despite these advances, an important gap remains in the analysis of honeycomb sandwich shells. Most available studies on honeycomb or auxetic-core shells focus on individual responses such as free vibration, buckling, impact, or blast behavior, while the structural boundaries are commonly represented by ideal simply supported, clamped, or free conditions. In practical structures, however, connections, joints, frames, and attachment systems possess finite stiffness, so the actual boundary behavior may lie between these classical limiting cases. Spring-based shell models further show that varying translational and rotational spring stiffnesses can represent a broad range of ideal and intermediate boundary states (Shi et al., 2016). Moreover, the combined use of a four-node cell-smoothed DSG formulation, an equivalent orthotropic re-entrant honeycomb core, and finite-stiffness elastic boundary conditions has not been sufficiently examined within a unified framework for both free-vibration and transient analyses. Consequently, the

coupled effects of shell curvature, auxetic cell geometry, and boundary flexibility remain insufficiently quantified for this class of sandwich shells.

To address this gap, the present study develops a novel cell-based smoothed discrete shear gap four-node (SM-DSG4) flat-shell element for the dynamic analysis of auxetic honeycomb sandwich shells with elastic boundary conditions. The sandwich structure consists of two isotropic face sheets and a re-entrant honeycomb core represented by equivalent orthotropic properties obtained from the unit-cell geometry. Elastic boundary conditions are modeled through distributed translational and rotational springs along the shell edges, allowing a continuous transition from flexible to strongly constrained supports. The principal methodological novelty lies in introducing cell-based strain smoothing into the membrane and bending strain fields of the conventional DSG4 element while retaining its original discrete shear gap formulation for transverse shear. The formulation is established for free vibration and transient dynamics within a common finite element framework. Its accuracy is assessed through benchmark problems involving laminated composite, sandwich, auxetic honeycomb, and elastically supported structures. Parametric studies then quantify the coupled effects of shell curvature, honeycomb inclination angle, conventional and elastic boundary conditions, and boundary stiffness on natural frequencies and time-dependent responses.

2 THEORETICAL FORMULATION

2.1 Geometry and equivalent material properties of the honeycomb sandwich shell



a) b)

Figure 1. Geometry of the honeycomb sandwich shell (a) and its auxetic honeycomb unit cell (b)

A curved sandwich shell with in-plane dimensions a and b, total thickness h, and radius of curvature R is considered, as illustrated in Fig. 1(a). The shell consists of three perfectly bonded material regions: the bottom face sheet B, the auxetic honeycomb core C, and the top face sheet T. The bottom and top face sheets are homogeneous and isotropic, whereas the cellular core is replaced by an equivalent homogeneous orthotropic continuum. Such an equivalent-continuum representation is commonly employed for honeycomb sandwich plates and shells to avoid explicitly discretizing the individual cell walls (Qing-Tian and Zhi-Chun, 2010; Tran et al., 2020).

Let h_B, h_C, and h_T denote the thicknesses of the bottom face sheet, honeycomb core, and top face sheet, respectively. Thus,

$$h = h_B + h_C + h_T. \tag{1}$$

Taking the reference midsurface of the complete sandwich shell as $z = 0$, the material interfaces are defined by

$$z_0 = -\frac{h}{2}, \qquad z_1 = z_0 + h_B, \qquad z_2 = z_1 + h_C, \qquad z_3 = \frac{h}{2}. \tag{2}$$

accordingly,

$$B:\ z_0 \le z \le z_1, \qquad C:\ z_1 \le z \le z_2, \qquad T:\ z_2 \le z \le z_3. \tag{3}$$

For the symmetric sandwich configuration considered in the main analyses,

$$h_B = h_T = h_f. \tag{4}$$

The face sheets are characterized by Young's modulus E_f, Poisson's ratio ν_f, shear modulus G_f, and mass density ρ_f, where

$$G_f = \frac{E_f}{2(1+\nu_f)}. \tag{5}$$

The re-entrant honeycomb unit cell is described by the inclined rib length l, vertical rib length h_r, wall thickness t, and signed inclination angle θ, as shown in Fig. 1(b). The notation h_r is used for the vertical rib length in order to distinguish it from the total shell thickness h. In the present convention, negative values of θ correspond to the re-entrant configurations considered in the numerical studies.

The cell walls are assumed to be made of an isotropic solid material with Young's modulus E_s, shear modulus G_s, Poisson's ratio ν_s, and density ρ_s, where

$$G_s = \frac{E_s}{2(1+\nu_s)}. \tag{6}$$

Following the cellular-material relations adopted for re-entrant honeycomb cores by Qing-Tian and Zhi-Chun (2010) and auxetic sandwich models (Tran et al., 2020), the equivalent in-plane Young's moduli are expressed as

$$E_1^C = E_s \left(\frac{t}{l}\right)^3 \frac{\cos\theta}{\left(\frac{h_r}{l}+\sin\theta\right)\sin^2\theta}, \tag{7}$$

and

$$E_2^C = E_s \left(\frac{t}{l}\right)^3 \frac{\left(\frac{h_r}{l}+\sin\theta\right)}{\cos^3\theta}. \tag{8}$$

The corresponding major in-plane Poisson's ratio is

$$\nu_{12}^C = \frac{\cos^2\theta}{\left(\frac{h_r}{l}+\sin\theta\right)\sin\theta}. \tag{9}$$

Equation (9) explicitly relates the effective Poisson's ratio to the unit-cell geometry and allows negative values for a re-entrant configuration.

To construct a symmetric orthotropic elastic constitutive tensor, the reciprocal Poisson's ratio is required to satisfy

$$\frac{\nu_{12}^C}{E_1^C} = \frac{\nu_{21}^C}{E_2^C}, \tag{10}$$

and therefore

$$\nu_{21}^C = \nu_{12}^C \frac{E_2^C}{E_1^C}. \tag{11}$$

The equivalent in-plane shear modulus is

$$G_{12}^C = E_s \left(\frac{t}{l}\right)^3 \frac{\frac{h_r}{l}+\sin\theta}{\left(\frac{h_r}{l}\right)^2\left(1+2\frac{h_r}{l}\right)\cos\theta}, \tag{12}$$

and the first transverse-shear modulus is

$$G_{13}^C = G_s \left(\frac{t}{l}\right) \frac{\cos\theta}{\frac{h_r}{l}+\sin\theta}. \tag{13}$$

Equations (7)-(9), (12), and (13) are the cellular-material relations adopted from Qing-Tian and Zhi-Chun (2010).

For consistency with the auxetic-honeycomb benchmark employed in the present study, the second transverse-shear modulus is taken from Tran et al. (2020) as

$$G_{23}^C = G_s \left(\frac{t}{l}\right) \frac{1+2\sin^2\theta}{2\cos\theta\left(\frac{h_r}{l}+\sin\theta\right)}. \tag{14}$$

The equivalent mass density is obtained from the relative amount of solid material contained in the representative cell (Qing-Tian and Zhi-Chun, 2010; Tran et al., 2020):

$$\rho_C = \rho_s \left(\frac{t}{l}\right) \frac{\frac{h_r}{l}+2}{2\cos\theta\left(\frac{h_r}{l}+\sin\theta\right)}. \tag{15}$$

After the unit-cell homogenization in Eqs. (7)-(15), the honeycomb core is treated as a continuous orthotropic material occupying the finite interval $z_1 \le z \le z_2$. Thus, the subsequent shell formulation does not integrate over individual honeycomb walls; it performs piecewise through-thickness integration over the bottom face sheet, homogenized core, and top face sheet.

For the isotropic face sheets $r = B, T$, the in-plane reduced stiffness matrix is

$$\mathbf{Q}_b^r = \begin{bmatrix} Q_{11}^r & Q_{12}^r & 0 \\ Q_{12}^r & Q_{22}^r & 0 \\ 0 & 0 & Q_{66}^r \end{bmatrix}, \tag{16}$$

where

$$Q_{11}^r = Q_{22}^r = \frac{E_f}{1-\nu_f^2}, \qquad Q_{12}^r = \frac{\nu_f E_f}{1-\nu_f^2}, \qquad Q_{66}^r = G_f. \tag{17}$$

Because the transverse-shear strain vector will subsequently be ordered as $\boldsymbol{\gamma}_s = \left[\gamma_{xz}, \gamma_{yz}\right]^T$, the corresponding transverse-shear stiffness matrix of the isotropic face sheets is defined consistently as

$$\mathbf{Q}_s^r = \begin{bmatrix} G_f & 0 \\ 0 & G_f \end{bmatrix}, \qquad r = B, T. \tag{18}$$

For the homogenized orthotropic honeycomb core,

$$\mathbf{Q}_b^C = \begin{bmatrix} Q_{11}^C & Q_{12}^C & 0 \\ Q_{12}^C & Q_{22}^C & 0 \\ 0 & 0 & Q_{66}^C \end{bmatrix}, \tag{19}$$

where

$$Q_{11}^C = \frac{E_1^C}{1-\nu_{12}^C \nu_{21}^C}, \qquad Q_{22}^C = \frac{E_2^C}{1-\nu_{12}^C \nu_{21}^C}, \tag{20a}$$

$$Q_{12}^C = \frac{\nu_{12}^C E_2^C}{1-\nu_{12}^C \nu_{21}^C} = \frac{\nu_{21}^C E_1^C}{1-\nu_{12}^C \nu_{21}^C}, \qquad Q_{66}^C = G_{12}^C. \tag{20b}$$

Consistently with the shear-strain ordering introduced above,

$$\mathbf{Q}_s^C = \begin{bmatrix} G_{13}^C & 0 \\ 0 & G_{23}^C \end{bmatrix}, \tag{21}$$

For compact notation in the following derivation, the material quantities through the complete sandwich thickness are therefore defined piecewise as

$$\mathbf{Q}_b(z) = \begin{cases} \mathbf{Q}_b^B, & z_0 \le z < z_1, \\ \mathbf{Q}_b^C, & z_1 \le z < z_2, \\ \mathbf{Q}_b^T, & z_2 \le z \le z_3, \end{cases} \tag{22}$$

$$\mathbf{Q}_s(z) = \begin{cases} \mathbf{Q}_s^B, & z_0 \le z < z_1, \\ \mathbf{Q}_s^C, & z_1 \le z < z_2, \\ \mathbf{Q}_s^T, & z_2 \le z \le z_3, \end{cases} \tag{23}$$

and

$$\rho(z)=\begin{cases}\rho_f, & z_0\le z<z_1,\\ \rho_C, & z_1\le z<z_2,\\ \rho_f, & z_2\le z\le z_3.\end{cases} \tag{24}$$

Equations (22)-(24) constitute the direct material input for the sectional stiffness and inertia quantities developed below.

The present study adopts an equivalent orthotropic continuum to describe the global structural response. This approach relies on the conventional scale-separation assumption that the characteristic cell dimensions are sufficiently small relative to the macroscopic deformation length scales. For the transient analyses, it is further assumed that the global structural response is dominated by macroscopic deformation modes, while local cell-wall dynamics, microstructural resonance, and wave-dispersion effects are not explicitly considered.

2.2 Weak form and general finite element formulation

The curved sandwich midsurface is represented by an assemblage of flat shell facets. A local Cartesian coordinate system (x, y, z) is attached to each facet, with the x- and y-axes lying in the midsurface and the z-axis normal to it. The spatial curvature of the shell is therefore represented by the different orientations of the local facet systems, while the deformation within each facet is described by first-order shear deformation theory (FSDT) (Nguyen-Thanh et al., 2008).

The generalized midsurface displacement vector contains three translations and three rotations and is written as

$$\mathbf{q}(x,y,t)=[u_0 \quad v_0 \quad w_0 \quad \theta_x \quad \theta_y \quad \theta_z]^T. \tag{25}$$

Here, θx and θy are the physical FSDT rotations, whereas θz is the drilling rotation introduced for the consistent assembly of non-coplanar flat-shell facets. The drilling rotation is an auxiliary finite element degree of freedom and does not contribute to the physical displacement or strain fields.

The three-dimensional displacement field through the thickness may be expressed compactly as

$$\mathbf{u}(x,y,z,t)=[u \quad v \quad w]^T=\mathbf{H}(z)\mathbf{q}, \qquad \mathbf{H}(z)=\begin{bmatrix}1&0&0&z&0&0\\0&1&0&0&z&0\\0&0&1&0&0&0\end{bmatrix}. \tag{26}$$

Accordingly, the in-plane and transverse-shear strain fields are decomposed as

$$\boldsymbol{\varepsilon}(x,y,z,t)=\boldsymbol{\varepsilon}_m+z\boldsymbol{\kappa}, \qquad \boldsymbol{\gamma}_s=[\gamma_{xz} \quad \gamma_{yz}]^T. \tag{27}$$

where the membrane strains, bending curvatures, and transverse-shear strains are

$$\begin{aligned}\boldsymbol{\varepsilon}_m&=[u_{0,x} \quad v_{0,y} \quad u_{0,y}+v_{0,x}]^T,\\ \boldsymbol{\kappa}&=[\theta_{x,x} \quad \theta_{y,y} \quad \theta_{x,y}+\theta_{y,x}]^T,\\ \boldsymbol{\gamma}_s&=[w_{0,x}+\theta_x \quad w_{0,y}+\theta_y]^T.\end{aligned} \tag{28}$$

Using the piecewise material matrices $\mathbf{Q}_b(z)$, $\mathbf{Q}_s(z)$, and $\rho(z)$ defined in Section 2.1, the sectional stiffness matrices are obtained directly by through-thickness integration:

$$\begin{aligned}\mathbf{A}&=\int_{z_0}^{z_3}\mathbf{Q}_b\,(z)\,dz, \qquad \mathbf{B}=\int_{z_0}^{z_3}z\,\mathbf{Q}_b(z)\,dz,\\ \mathbf{D}&=\int_{z_0}^{z_3}z^2\,\mathbf{Q}_b(z)\,dz, \quad \mathbf{D}_s=k_s\int_{z_0}^{z_3}\mathbf{Q}_s\,(z)\,dz.\end{aligned} \tag{29}$$

The integrations in Eq. (29) are evaluated piecewise over the bottom face sheet, homogenized honeycomb core, and top face sheet. The corresponding sectional constitutive relation is

$$\begin{bmatrix}\mathbf{N}\\ \mathbf{M}\\ \mathbf{Q}\end{bmatrix}=\begin{bmatrix}\mathbf{A}&\mathbf{B}&\mathbf{0}\\ \mathbf{B}&\mathbf{D}&\mathbf{0}\\ \mathbf{0}&\mathbf{0}&\mathbf{D}_s\end{bmatrix}\begin{bmatrix}\boldsymbol{\varepsilon}_m\\ \boldsymbol{\kappa}\\ \boldsymbol{\gamma}_s\end{bmatrix}. \tag{30}$$

For the symmetric sandwich configuration considered in the main analyses, the identical face sheets and symmetric core placement give

$$\mathbf{B}=\mathbf{0}. \tag{31}$$

The sectional inertia matrix associated with the six-component generalized vector follows from the same through-thickness description:

$$\mathbf{m} = \int_{z_0}^{z_3} \rho\,(z)\,\mathbf{H}^T(z)\mathbf{H}(z)\,dz. \tag{32}$$

The zero contribution associated with θz follows automatically from the zero sixth column of H(z); therefore, no fictitious physical inertia is assigned to the drilling degree of freedom.

A transverse pressure acting along the local shell normal is written in the general separable form

$$p(x,y,t) = p_0\,\Psi(x,y)\,F(t). \tag{33}$$

where p_0 is a reference pressure amplitude, $\Psi(x,y)$ is the spatial distribution, and F(t) is the prescribed time history. The particular triangular, sinusoidal, and blast-type histories are specified only in the corresponding numerical studies.

Applying Hamilton's principle and integrating the inertial term by parts in time gives the following continuum weak statement:

$$\begin{gathered}\int_\Omega (\delta\boldsymbol{\varepsilon}_m^T\mathbf{N} + \delta\boldsymbol{\kappa}^T\mathbf{M} + \delta\boldsymbol{\gamma}_s^T\mathbf{Q})\,d\Omega + \int_\Omega \delta\,\mathbf{q}^T\mathbf{m}\,\ddot{\mathbf{q}}\,d\Omega \\ +\delta\Pi_\Gamma - \int_\Omega \delta\,\mathbf{q}^T\mathbf{e}_w\,p(x,y,t)\,d\Omega = 0, \\ \mathbf{e}_w = [0 \quad 0 \quad 1 \quad 0 \quad 0 \quad 0]^T.\end{gathered} \tag{34}$$

In Eq. (34), the boundary contribution $\delta\Pi_\Gamma$ accounts for the distributed spring terms associated with the elastic boundary conditions and is specified in Section 2.3. No physical damping term is introduced in the present formulation.

For the general finite element discretization, the generalized displacement field over an element is interpolated as

$$\mathbf{q}^h(x,y,t) = \sum_{i=1}^{n_e} N_i\,(x,y)\mathbf{d}_i(t) = \mathbf{N}_q\mathbf{d}_e. \tag{35}$$

and the membrane, bending, and transverse-shear strain measures may be written in the generic matrix form

$$\boldsymbol{\varepsilon}_m = \mathbf{B}_m\mathbf{d}_e, \qquad \boldsymbol{\kappa} = \mathbf{B}_b\mathbf{d}_e, \qquad \boldsymbol{\gamma}_s = \mathbf{B}_s\mathbf{d}_e. \tag{36}$$

Substitution of Eq. (36) into the weak form yields the structural element stiffness matrix

$$\begin{gathered}\mathbf{K}_e^{\mathrm{str}} = \int_{\Omega_e} (\mathbf{B}_m^T\mathbf{A}\mathbf{B}_m + \mathbf{B}_m^T\mathbf{B}\mathbf{B}_b + \mathbf{B}_b^T\mathbf{B}\mathbf{B}_m \\ +\mathbf{B}_b^T\mathbf{D}\mathbf{B}_b + \mathbf{B}_s^T\mathbf{D}_s\mathbf{B}_s)\,d\Omega.\end{gathered} \tag{37}$$

whereas the consistent element mass matrix and the pressure-load vector are, respectively,

$$\mathbf{M}_e = \int_{\Omega_e} \mathbf{N}_q^T\,\mathbf{m}\mathbf{N}_q\,d\Omega. \tag{38}$$

$$\mathbf{f}_e(t) = \int_{\Omega_e} \mathbf{N}_q^T\,\mathbf{e}_w\,p(x,y,t)\,d\Omega. \tag{39}$$

At this stage, Bm, Bb, and Bs are generic strain-displacement operators. Their specific construction for the four-node DSG4 and the proposed smoothed DSG4 element is introduced only in Section 3. This separation allows the continuum shell formulation and the element-specific numerical treatment to remain clearly distinguished.

2.3 Elastic boundary condition model

To represent the finite stiffness of joints, frames, and attachment systems, distributed translational and rotational springs are assigned independently along selected shell edges, as illustrated in Fig. 2. This spring-based model provides a continuous transition between free boundaries and increasingly constrained support conditions.

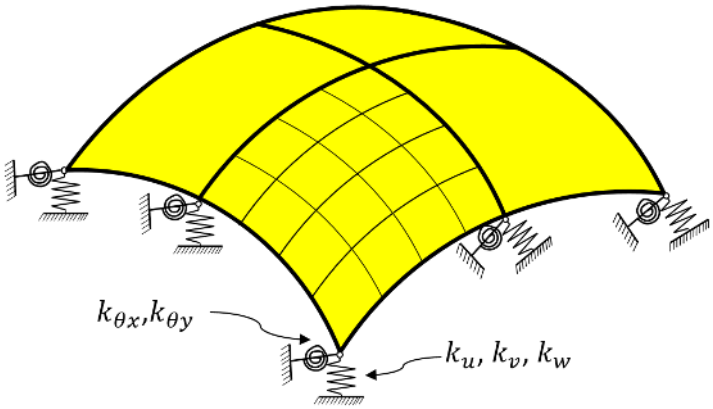


Figure 2. Shell model with elastic boundary conditions

For a boundary segment Γs subjected to elastic boundary conditions, the spring-stiffness matrix associated with the six-component flat-shell vector is defined as

$$\mathbf{K}_\Gamma = \mathrm{diag}\left(k_u, k_v, k_w, k_{\theta_x}, k_{\theta_y}, 0\right). \tag{40}$$

The zero sixth entry reflects the auxiliary character of the drilling rotation θz; no physical boundary-spring energy is assigned to this degree of freedom. The elastic potential energy and its first variation are

$$\Pi_\Gamma = \frac{1}{2}\int_{\Gamma_s} \mathbf{q}_\Gamma^T \mathbf{K}_\Gamma \mathbf{q}_\Gamma \, d\Gamma, \qquad \delta\Pi_\Gamma = \int_{\Gamma_s} \delta\, \mathbf{q}_\Gamma^T \mathbf{K}_\Gamma \mathbf{q}_\Gamma \, d\Gamma. \tag{41}$$

After finite element interpolation along a restrained element edge, the corresponding boundary-stiffness contribution is

$$\mathbf{K}_e^\Gamma = \int_{\Gamma_s^e} \mathbf{N}_\Gamma^T \mathbf{K}_\Gamma \mathbf{N}_\Gamma \, d\Gamma. \tag{42}$$

For comparison between different shell sizes and stiffness levels, the translational and rotational spring parameters are nondimensionalized as

$$\bar{k}_u = \frac{k_u L^3}{D_0}, \qquad \bar{k}_v = \frac{k_v L^3}{D_0}, \qquad \bar{k}_w = \frac{k_w L^3}{D_0},$$
$$\bar{k}_{\theta_x} = \frac{k_{\theta_x} L}{D_0}, \qquad \bar{k}_{\theta_y} = \frac{k_{\theta_y} L}{D_0}. \tag{43}$$

Here, L is the characteristic length of the supported edge and D0 is the reference bending rigidity. A zero spring parameter leaves the associated generalized displacement free, a finite positive value represents a finite-stiffness elastic boundary condition, and a sufficiently large value approaches the corresponding classical constrained condition. The same formulation is applied independently to each shell edge, allowing different boundary-stiffness combinations to be prescribed without changing the element formulation.

Boundary-spring contributions are assembled by consistent interpolation along each supported edge and integration over its physical length. Translational and rotational spring coefficients are defined per unit boundary length, with the associated energy terms assembled into the global stiffness matrix. The zero- and large-stiffness limits, together with boundary-mesh refinement, are evaluated in Section 4.1.

3 FORMULATION OF THE FOUR-NODE FLAT-SHELL SM-DSG4 ELEMENT

3.1 DSG4 formulation

Following the original DSG concept of Bletzinger et al. (2000), the standard bilinear four-node flat-shell interpolation is retained for the displacement and rotation variables, whereas the transverse-shear field is reconstructed from

interpolated discrete shear gaps. Each node contains the six local degrees of freedom introduced in Section 2.2, and the nodal displacement vector is written as

$$\mathbf{d}_i = [u_i \quad v_i \quad w_i \quad \theta_{xi} \quad \theta_{yi} \quad \theta_{zi}]^T \tag{44}$$

The element displacement vector is assembled as

$$\mathbf{d}_e = [\mathbf{d}_1^T \quad \mathbf{d}_2^T \quad \mathbf{d}_3^T \quad \mathbf{d}_4^T]^T \tag{45}$$

In the parent coordinates (ξ, η), the bilinear shape functions are defined by Eq. (46), where the parent coordinates of nodes 1–4 are (−1,−1), (1,−1), (1,1), and (−1,1), respectively; the generalized displacement field is interpolated by the same functions:

$$N_i(\xi,\eta) = 1/4\,(1+\xi_i\xi)(1+\eta_i\eta), \quad i = 1,\ldots,4; \qquad \mathbf{q}^h(\xi,\eta,t) = \sum_{i=1}^{4} N_i\,\mathbf{d}_i(t) = \mathbf{N}_q\mathbf{d}_e \tag{46}$$

The membrane and bending fields retain the conventional compatible operators,

$$\boldsymbol{\varepsilon}_m = \mathbf{B}_m\mathbf{d}_e, \qquad \boldsymbol{\kappa} = \mathbf{B}_b\mathbf{d}_e \tag{47}$$

where the two matrices in Eq. (47) are the conventional membrane and bending strain-displacement operators. With the FSDT sign convention adopted in Section 2.2, the covariant transverse-shear components in the parent coordinates are

$$\begin{bmatrix}\gamma_{\xi z}^h \\ \gamma_{\eta z}^h\end{bmatrix} = \begin{bmatrix}w_{,\xi}^h + x_{,\xi}\theta_x^h + y_{,\xi}\theta_y^h \\ w_{,\eta}^h + x_{,\eta}\theta_x^h + y_{,\eta}\theta_y^h\end{bmatrix} \tag{48}$$

The DSG construction does not directly interpolate the compatible shear strains in Eq. (48). Instead, the corresponding shear deformation is represented by discrete shear gaps. Taking an arbitrary reference value as the integration constant, the nodal shear gaps are obtained by integrating the covariant shear strains along the appropriate element-coordinate lines (Bletzinger et al., 2000):

$$\Delta w_{\xi i}^{\gamma} = \int_{\Gamma_{\xi i}} \gamma_{\xi z}^h\, d\xi, \qquad \Delta w_{\eta i}^{\gamma} = \int_{\Gamma_{\eta i}} \gamma_{\eta z}^h\, d\eta \tag{49}$$

Only differences of the shear gaps are relevant; therefore, the additive integration constants may be chosen arbitrarily. The discrete shear-gap fields are then interpolated with the same bilinear shape functions as the displacement field,

$$\Delta w_{\xi}^{\gamma,h} = \sum_{i=1}^{4} N_i\,\Delta w_{\xi i}^{\gamma}, \qquad \Delta w_{\eta}^{\gamma,h} = \sum_{i=1}^{4} N_i\,\Delta w_{\eta i}^{\gamma} \tag{50}$$

and the modified transverse-shear strains are recovered by differentiating the interpolated shear-gap fields,

$$\tilde{\gamma}_{\xi z}^{\mathrm{DSG}} = \frac{\partial \Delta w_{\xi}^{\gamma,h}}{\partial \xi} = \sum_{i=1}^{4} N_{i,\xi}\,\Delta w_{\xi i}^{\gamma}, \qquad \tilde{\gamma}_{\eta z}^{\mathrm{DSG}} = \frac{\partial \Delta w_{\eta}^{\gamma,h}}{\partial \eta} = \sum_{i=1}^{4} N_{i,\eta}\,\Delta w_{\eta i}^{\gamma} \tag{51}$$

For a bilinear four-node quadrilateral, this DSG procedure produces the linear-constant natural shear distributions reported by Bletzinger et al. (2000), which are identical to the classical ANS/MITC4 interpolation. Denoting the midside sampling points by A=(0,−1), B=(1,0), C=(0,1), and D=(−1,0), these distributions may be written as

$$\begin{bmatrix}\tilde{\gamma}_{\xi z}^{\mathrm{DSG}}(\xi,\eta) \\ \tilde{\gamma}_{\eta z}^{\mathrm{DSG}}(\xi,\eta)\end{bmatrix} = 1/2\begin{bmatrix}(1-\eta)\gamma_{\xi z}^{A} + (1+\eta)\gamma_{\xi z}^{C} \\ (1-\xi)\gamma_{\eta z}^{D} + (1+\xi)\gamma_{\eta z}^{B}\end{bmatrix} \tag{52}$$

Accordingly, the natural-coordinate DSG shear vector is expressed in matrix form as

$$\tilde{\boldsymbol{\gamma}}_n^{\mathrm{DSG}} = \left[\tilde{\gamma}_{\xi z}^{\mathrm{DSG}} \quad \tilde{\gamma}_{\eta z}^{\mathrm{DSG}}\right]^T = \mathbf{B}_{s,n}^{\mathrm{DSG}}\mathbf{d}_e \tag{53}$$

The local Cartesian transverse-shear vector used in the constitutive relation of Section 2.2 follows from the standard covariant transformation,

$$\boldsymbol{\gamma}_s^{\mathrm{DSG}} = \mathbf{J}^{-1}\tilde{\boldsymbol{\gamma}}_n^{\mathrm{DSG}} = \mathbf{B}_s^{\mathrm{DSG}}\mathbf{d}_e, \qquad \mathbf{J} = \begin{bmatrix}x_{,\xi} & y_{,\xi} \\ x_{,\eta} & y_{,\eta}\end{bmatrix} \tag{54}$$

Thus, the conventional DSG4 element retains the standard membrane and bending operators while replacing the directly interpolated transverse-shear field by the DSG operator defined in Eq. (54). This separation is retained in the proposed smoothed element.

3.2 Formulation of the SM-DSG4 flat-shell element

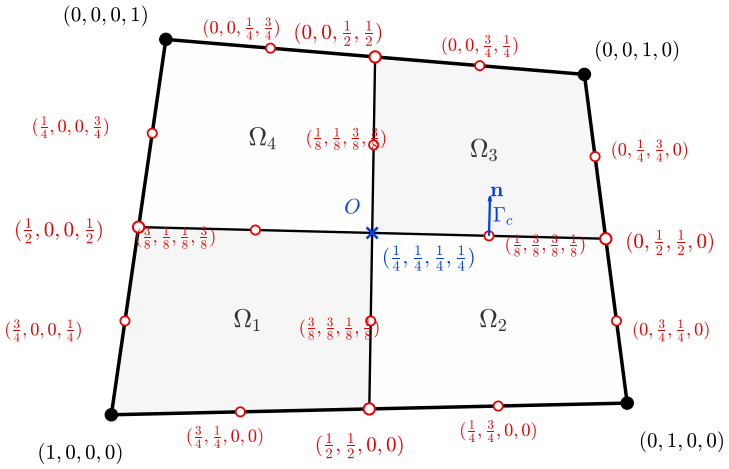


Figure 3. Schematic of the SM-DSG4 formulation

The proposed SM-DSG4 element is developed by introducing cell-based strain smoothing into the membrane and bending strain fields of the conventional DSG4 element, while retaining its original discrete shear gap interpolation for transverse shear. The smoothing procedure follows the cell-based approach of Nguyen-Thanh et al. (2008),

$$\Omega_e = \bigcup_{C=1}^{4} \Omega_C, \qquad \Omega_C \cap \Omega_D = \varnothing \quad (C \neq D) \tag{55}$$

Each smoothing cell is characterized by its own area and boundary, as illustrated in Fig. 3. A constant smoothing function is adopted over each cell, and application of the divergence theorem converts the area average of the compatible shape-function gradients into the boundary form in Eq. (56):

$$\widetilde{N}_{i,\alpha}^{C} = \frac{1}{A_C}\int_{\Omega_C} N_{i,\alpha}\, d\Omega = \frac{1}{A_C}\int_{\Gamma_C} N_i\, n_\alpha\, d\Gamma, \qquad \alpha \in \{x, y\} \tag{56}$$

The boundary integral in Eq. (56) involves the two components of the outward unit normal to the smoothing-cell boundary. For the six-degree-of-freedom nodal ordering used in this study, the smoothed membrane matrix associated with node i is

$$\widetilde{\mathbf{B}}_{mi}^{C} = \begin{bmatrix} \widetilde{N}_{i,x}^{C} & 0 & 0 & 0 & 0 & 0 \\ 0 & \widetilde{N}_{i,y}^{C} & 0 & 0 & 0 & 0 \\ \widetilde{N}_{i,y}^{C} & \widetilde{N}_{i,x}^{C} & 0 & 0 & 0 & 0 \end{bmatrix}, \qquad \widetilde{\mathbf{B}}_{m}^{C} = [\widetilde{\mathbf{B}}_{m1}^{C} \quad \widetilde{\mathbf{B}}_{m2}^{C} \quad \widetilde{\mathbf{B}}_{m3}^{C} \quad \widetilde{\mathbf{B}}_{m4}^{C}] \tag{57}$$

and the corresponding smoothed bending matrix is

$$\widetilde{\mathbf{B}}_{bi}^{C} = \begin{bmatrix} 0 & 0 & 0 & \widetilde{N}_{i,x}^{C} & 0 & 0 \\ 0 & 0 & 0 & 0 & \widetilde{N}_{i,y}^{C} & 0 \\ 0 & 0 & 0 & \widetilde{N}_{i,y}^{C} & \widetilde{N}_{i,x}^{C} & 0 \end{bmatrix}, \qquad \widetilde{\mathbf{B}}_{b}^{C} = [\widetilde{\mathbf{B}}_{b1}^{C} \quad \widetilde{\mathbf{B}}_{b2}^{C} \quad \widetilde{\mathbf{B}}_{b3}^{C} \quad \widetilde{\mathbf{B}}_{b4}^{C}] \tag{58}$$

The cell-based membrane-bending contribution is therefore obtained by summing the smoothed contributions from the four cells,

$$\mathbf{K}_{mb}^{e} = \sum_{C=1}^{4} A_C \left[\left(\widetilde{\mathbf{B}}_{m}^{C}\right)^T \mathbf{A} \widetilde{\mathbf{B}}_{m}^{C} + \left(\widetilde{\mathbf{B}}_{m}^{C}\right)^T \mathbf{B} \widetilde{\mathbf{B}}_{b}^{C} + \left(\widetilde{\mathbf{B}}_{b}^{C}\right)^T \mathbf{B} \widetilde{\mathbf{B}}_{m}^{C} + \left(\widetilde{\mathbf{B}}_{b}^{C}\right)^T \mathbf{D} \widetilde{\mathbf{B}}_{b}^{C} \right] \tag{59}$$

where $\mathbf{A}$, $\mathbf{B}$, and $\mathbf{D}$ are the extensional, membrane-bending coupling, and bending stiffness matrices defined in Section 2.2.

$$\mathbf{K}_s^e = \int_{\Omega_e} (\mathbf{B}_s^{\mathrm{DSG}})^T \, \mathbf{D}_s \mathbf{B}_s^{\mathrm{DSG}} \, d\Omega \tag{60}$$

The sectional transverse-shear stiffness matrix in Eq. (60) is the one defined in Section 2.2. Hence, the structural stiffness matrix of the proposed element is

$$\mathbf{K}_e = \mathbf{K}_{mb}^e + \mathbf{K}_s^e \tag{61}$$

The consistent element mass matrix follows directly from the sectional inertia relation established in the weak form,

$$\mathbf{M}^e = \int_{\Omega_e} \mathbf{N}_q^T \, \mathbf{m} \mathbf{N}_q \, d\Omega \tag{62}$$

The stiffness contribution associated with the elastic boundary conditions along the supported element edges is

$$\mathbf{K}_\Gamma^e = \int_{\Gamma_s^e} \mathbf{N}_\Gamma^T \, \mathbf{K}_\Gamma \mathbf{N}_\Gamma \, d\Gamma \tag{63}$$

and the consistent element load vector associated with the transverse pressure is

$$\mathbf{f}^e(t) = \int_{\Omega_e} \mathbf{N}_q^T \, \mathbf{e}_w \, p(x, y, t) \, d\Omega \tag{64}$$

Because the physical strain operators provide no stiffness for the drilling rotation, a small numerical stabilization is added only to the drilling-rotation diagonal terms. Following Nguyen-Thanh et al. (2008),

$$k_{\theta_z}^e = \alpha_d \max_i(K_{ii}^e), \qquad \alpha_d = 10^{-3} \tag{65}$$

The stabilization in Eq. (65) suppresses the spurious zero-energy drilling mode without modifying the physical FSDT strain fields. Finally, the local element matrices and load vector are transformed to the global coordinate system using the block transformation matrix defined in Eq. (66), which is constructed from the local orthonormal basis of each flat facet,

$$\mathbf{K}_e^G = \mathbf{T}_e^T(\mathbf{K}^e + \mathbf{K}_d^e + \mathbf{K}_\Gamma^e)\mathbf{T}_e, \qquad \mathbf{M}_e^G = \mathbf{T}_e^T \mathbf{M}^e \mathbf{T}_e, \qquad \mathbf{f}_e^G = \mathbf{T}_e^T \mathbf{f}^e \tag{66}$$

The resulting SM-DSG4 element therefore combines cell-smoothed membrane and bending contributions with the locking-resistant DSG4 transverse-shear field, while retaining the original six-degree-of-freedom flat-shell kinematics and introducing no additional physical nodal variables.

After assembly of all transformed element contributions, the global semi-discrete equation of motion is obtained as

$$\mathbf{M}\ddot{\mathbf{d}}(t) + \mathbf{K}\mathbf{d}(t) = \mathbf{F}(t), \tag{67}$$

Here, $\mathbf{M}$ is the assembled mass matrix, while $\mathbf{K}$ is the effective global stiffness matrix containing the structural SM-DSG4 stiffness, elastic-boundary stiffness, and drilling-stabilization contributions. No physical damping term is introduced in the present formulation.

For free vibration, the external load is set to zero. Assuming harmonic motion, Eq. (67) yields the generalized eigenvalue problem

$$(\mathbf{K} - \omega^2 \mathbf{M})\boldsymbol{\Phi} = \mathbf{0}, \tag{68}$$

where ω is the natural circular frequency and Φ is the corresponding mode-shape vector.

For transient analysis, Eq. (67) is integrated in the time domain by the Newmark average-acceleration scheme. The displacement update is

$$\mathbf{d}_{n+1} = \mathbf{d}_n + \Delta t \, \dot{\mathbf{d}}_n + \Delta t^2 \left[(1/2 - \beta)\ddot{\mathbf{d}}_n + \beta \ddot{\mathbf{d}}_{n+1}\right], \tag{69}$$

and the velocity update is

$$\dot{\mathbf{d}}_{n+1} = \dot{\mathbf{d}}_n + \Delta t \left[(1 - \gamma_N)\ddot{\mathbf{d}}_n + \gamma_N \ddot{\mathbf{d}}_{n+1}\right]. \tag{70}$$

For the average-acceleration scheme, the Newmark parameters are selected as

$$\beta = 1/4\,, \qquad \gamma_N = 1/2. \tag{71}$$

These equations provide the common discrete framework used for the free-vibration and transient analyses reported in Section 4.

4 COMPUTATIONAL RESULTS AND DISCUSSION

4.1 Verification of accuracy and mesh-distortion robustness

First, to assess robustness against mesh distortion, the interior nodes of each N × N mesh are perturbed in the projected x-direction according to $x_i^* = x_i + \alpha r_i \Delta x$, $y_i^* = y_i$. Here, $r_i \in [-1,1]$ is a fixed dimensionless perturbation coefficient, $\Delta x = a/N$, and α controls the distortion magnitude. Boundary nodes are kept unchanged, and each perturbed interior node is projected back onto the spherical midsurface. For each mesh density, one fixed perturbation pattern is scaled by α, and exactly the same distorted geometry is used for DSG4 and SM-DSG4. The regular mesh corresponds to $\alpha = 0$, whereas Fig. 4 reports the representative distorted case $\alpha = 0.3$.

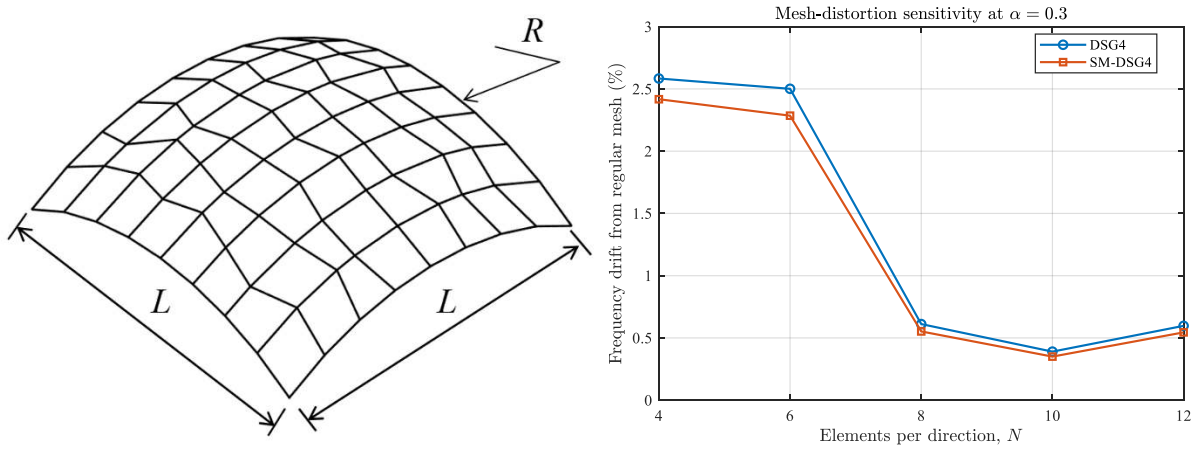


Figure 4. Effect of mesh density on the distortion-induced fundamental-frequency drift of DSG4 and SM-DSG4 elements at α = 0.3

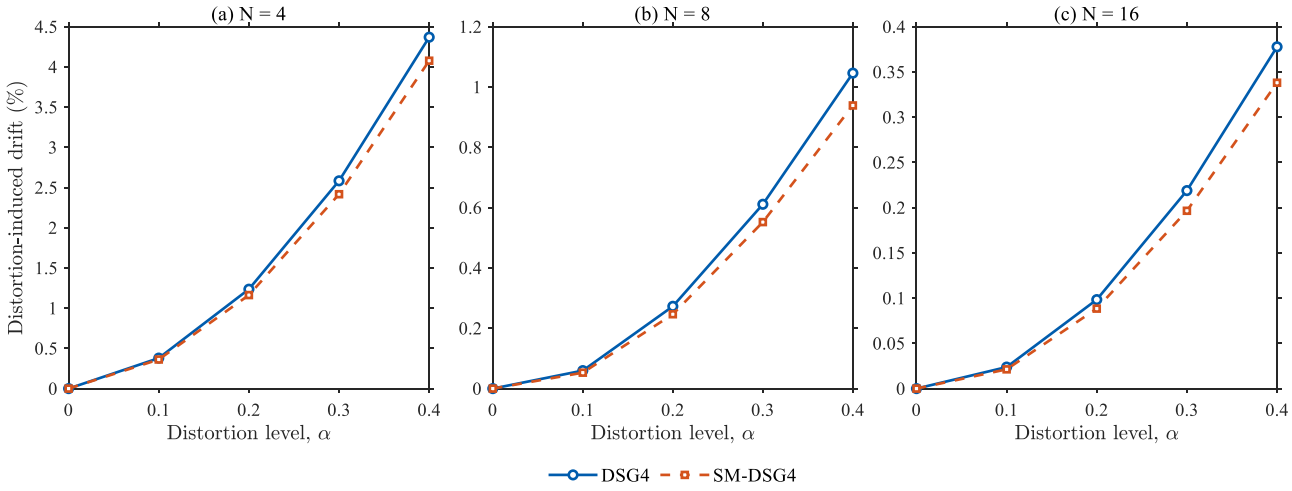


Figure 5. Mesh-distortion-induced fundamental-frequency drift of the DSG4 and SM-DSG4 elements for different distortion levels

Figure 4 evaluates the mesh-distortion sensitivity of the conventional DSG4 and proposed SM-DSG4 elements using the laminated spherical-shell benchmark configuration considered by Sayyad and Ghugal (2019), with $[0°/90°/0°]$, $R/a = 5$, and $a/h = 100$. The distortion-induced frequency drift is defined relative to the corresponding regular-mesh solution as $e_{dist} = \frac{|\overline{\Omega}(\alpha) - \overline{\Omega}(0)|}{\overline{\Omega}(0)} \times 100\%$, thereby isolating the influence of element distortion from the baseline discretization error. For all considered mesh densities, the SM-DSG4 element exhibits a smaller frequency drift than the conventional DSG4 element, i.e.,$e_{dist}{}^{SM-DSG4} < e_{dist}{}^{DSG4}$. At $\alpha = 0.3$, the smoothing treatment reduces the distortion-induced frequency drift by approximately 6.4–10.3% over the investigated meshes. The difference is particularly evident for coarse discretizations, for which mesh distortion produces a stronger perturbation of the numerical stiffness. As the mesh density increases, the frequency drift of both formulations decreases substantially, while the SM-DSG4 solution remains consistently less sensitive to element distortion. These results demonstrate that strain

smoothing improves the mesh-distortion robustness of the DSG4 shell formulation without changing its underlying transverse-shear treatment.

Figure 5 further examines the effect of mesh distortion on the fundamental-frequency drift for three mesh densities ($N = 4, 8, 16$) over distortion levels ranging from 0 to 0.4. For all three meshes, the frequency drift increases nonlinearly with increasing distortion, while the proposed SM-DSG4 element consistently exhibits smaller deviations than the conventional DSG4 element. The difference becomes more pronounced at higher distortion levels, particularly for coarse meshes. As the mesh is refined, the frequency drift decreases for both formulations, indicating that strain smoothing improves the robustness of the computed natural frequencies against mesh distortion.

The accuracy of the proposed formulation is further assessed through the free-vibration analysis of laminated composite spherical shells summarized in Table 1. Two cross-ply configurations are considered, namely the two-layer antisymmetric laminate $0°/90°$ and the three-layer symmetric laminate $0°/90°/0°$. The nondimensional fundamental frequencies obtained from the present model are compared with the reference solutions of Sayyad and Ghugal (2019) for different curvature ratios $\mathrm{R/a} = 5,10,20,50,100$, and thickness ratios $\mathrm{a/h} = 5,10,20,50,100$. The results in Table 1 show good agreement between the present formulation and the reference solutions of Sayyad and Ghugal (2019) for the free-vibration analysis of laminated composite spherical shells.

Table 1. Comparison of dimensionless fundamental frequencies for laminated composite spherical shells $\bar{\omega} = \omega \frac{a^2}{h}\sqrt{\frac{\rho}{E_2}}$

$0^o/90^o$						
R/a	Theory	a/h				
		5	10	20	50	100
5	Present	7.5029	9.2957	10.9273	16.7442	29.0373
	Sayyad and Ghugal (2019)	7.7139	9.3675	10.9318	16.7076	29.0276
10	Present	7.4335	9.0230	9.8834	11.8614	16.7952
	Sayyad and Ghugal (2019)	7.6482	9.0991	9.8978	11.8575	16.8222
20	Present	7.4161	8.9535	9.6041	10.2804	11.8935
	Sayyad and Ghugal (2019)	7.6316	9.0303	9.6202	10.2828	11.9227
50	Present	7.4112	8.9339	9.5244	9.7918	10.1023
	Sayyad and Ghugal (2019)	7.6269	9.0109	9.5408	9.7958	10.1316
100	Present	7.4105	8.9311	9.5129	9.7200	9.8197
	Sayyad and Ghugal (2019)	7.6263	9.0081	9.5294	9.7242	9.8491
$0^o/90^o/0^o$						
5	Present	8.7027	12.4464	15.2201	20.2980	31.2122
	Sayyad and Ghugal (2019)	9.1605	12.7782	15.3454	20.2981	31.2270
10	Present	8.6460	12.2604	14.5201	16.5615	20.4475
	Sayyad and Ghugal (2019)	9.1095	12.5953	14.6482	16.5838	20.4962
20	Present	8.6317	12.2134	14.3394	15.4845	16.6956
	Sayyad and Ghugal (2019)	9.0966	12.5489	14.4675	15.5097	16.7459

$0^o/90^o$						
R/a	Theory	a/h				
		5	10	20	50	100
50	Present	8.6277	12.2002	14.2883	15.1691	15.4822
	Sayyad and Ghugal (2019)	9.0930	12.5358	14.4164	15.1949	15.5323
100	Present	8.6272	12.1983	14.2810	15.1235	15.3010
	Sayyad and Ghugal (2019)	9.0924	12.5339	14.4091	15.1493	15.3510

To verify the applicability of the formulation to auxetic honeycomb sandwich structures, Table 2 presents the validation results of the first natural frequency of a sandwich panel with an auxetic honeycomb core. The geometric parameters of the plate are given as: total thickness $h = 0.1\,m$, plate dimensions $a = b = 20h$, and thickness ratio $h_c/\,h_f = 1.5$, with equal face sheet thicknesses. The plate is made of aluminum material with mechanical properties: $E = 69\,GPa, G = 26\,GPa, \nu = 0.33$, and $\rho = 2700\,kg/m^3$. The auxetic honeycomb core is characterized by $t/l = 0.1385$, while the geometric parameters vary as $h/l = 0.5, 1, 2, 4$ and $\theta = -10°, -35°, -55°, -80°$. The present results are compared with those reported by Tran et al. (2020) to evaluate the accuracy and reliability of the proposed finite element formulation. The present results agree well with those of Tran et al. (2020); all relative errors remain below 2%, and most are below 1%.

Table 2. The first natural frequency of a sandwich panel with an auxetic honeycomb core

h/l	θ^o	Present	Tran et al. (2020)	Error (%)
0.5	-10	150.9770	150.0868	0.5931
	-35	172.2555	172.3232	0.0393
	-55	158.8062	158.6420	0.1035
	-80	165.5878	166.0869	0.3005
1	-10	152.0365	151.6094	0.2817
	-35	149.9908	149.7829	0.1388
	-55	143.0122	142.8576	0.1082
	-80	58.7489	58.7157	0.0565
2	-10	152.4312	152.1649	0.1750
	-35	151.9051	151.7055	0.1316
	-55	150.9871	150.7676	0.1456
	-80	146.0402	144.8534	0.8193
4	-10	152.6169	152.4068	0.1378
	-35	152.4237	152.1957	0.1498
	-55	152.0709	151.7532	0.2093
	-80	151.4361	148.7206	1.8259

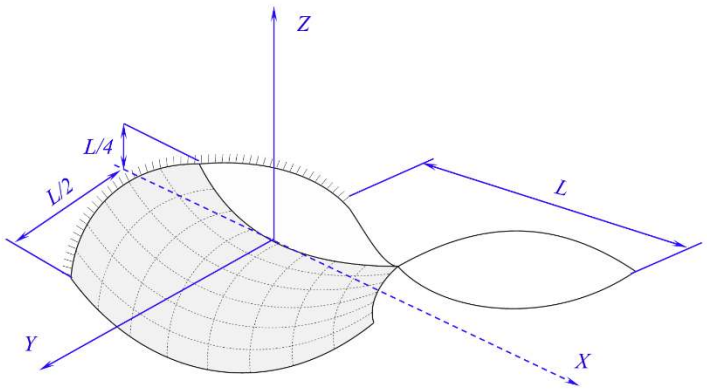


Figure 6. Model geometry of hyperbolic paraboloid shell

To investigate the convergence behavior and shear-locking alleviation of the proposed SM-DSG4 element, the partly clamped hyperbolic paraboloid shell benchmark studied by Nguyen-Van et al. (2009) is considered. The shell is clamped along one edge and free along the remaining three edges, and is subjected to a uniformly distributed self-weight load, with $g = 1\ m/s^2$ as shown in Fig. 6. The isotropic material properties are $E = 2 \times 10^{11}$ Pa, $\nu = 0.3$, and $\rho = 8000\ kg/m^3$. Taking advantage of symmetry, only one half of the shell is discretized using $N \times N/2$ quadrilateral elements, where $N = 8, 16, 32, 48,$ and 64. Two thickness-to-length ratios, $t/L = 1/100$ and $1/1000$, are examined, and the vertical displacement at point A is compared with the published results obtained using the MISQ24 element developed by Nguyen-Van et al. (2009). As shown in Table 3, the proposed element exhibits satisfactory convergence for both thickness ratios, with relative differences of 0.974% and 0.261%, respectively, at the finest mesh. These results provide numerical evidence of the effectiveness of the proposed formulation in alleviating shear locking in the thin-shell regime.

Table 3. Comparison of vertical displacement at point A between the present SM-DSG4 element and the published MISQ24 results

t/L	Mesh	MISQ24	SM-DSG4	Difference (%)
1/100	8 × 4	9.90880E−05	9.74684E−05	−1.635
	16 × 8	9.46810E−05	9.48548E−05	+0.184
	32 × 16	9.36650E−05	9.44127E−05	+0.798
	48 × 24	9.35010E−05	9.43687E−05	+0.928
	64 × 32	9.34530E−05	9.43635E−05	+0.974
1/1000	8 × 4	7.12090E−03	6.78716E−03	−4.687
	16 × 8	6.71290E−03	6.46345E−03	−3.716
	32 × 16	6.46770E−03	6.40152E−03	−1.023
	48 × 24	6.42640E−03	6.39652E−03	−0.465
	64 × 32	6.41300E−03	6.39627E−03	−0.261

Note: Difference (%) = [(SM-DSG4 − MISQ24) / MISQ24] × 100. All displacement values are in metres.

The implementation of the elastic boundary conditions is subsequently verified using the first natural frequency parameter of a three-layer angle-ply laminated plate. The laminate stacking sequence is defined as $(\theta/-\theta/\theta), \theta = 15°,\ 30°,\ 45°$. A square plate is considered with the geometric ratios $\frac{a}{b} = 1, \frac{h}{b} = 0.1$. The orthotropic material properties of each lamina are taken as $\frac{E_{11}}{E_{22}} = 40, \frac{G_{12}}{E_{22}} = \frac{G_{13}}{E_{22}} = 0.6, \frac{G_{23}}{E_{22}} = 0.5, \nu_{12} = 0.25$. The nondimensional first natural frequency parameter used for comparison is $\bar{\omega}_1 = \omega_1 \frac{b^2}{\pi^2 h}\sqrt{\frac{\rho}{E_{22}}}$. In the present implementation, the in-plane displacements u and v are not constrained, while the transverse displacement w is restrained along all edges by distributed springs of stiffness K. The rotational degrees of freedom are restrained anisotropically, where θ_x is controlled along the edges $x = 0$ and $x = a$, and θ_y is controlled along the edges $y = 0$ and $y = b$. This configuration directly corresponds to the adopted stiffness matrix k_{ij} in the numerical model and enables a realistic representation of partially restrained boundaries. The

dimensionless boundary-stiffness parameter is varied as $k = 10^1,\ 10^2,\ 10^3,\ 10^4,\ 10^6,\ 10^8$. The results reported in Table 4 demonstrate that the present method provides satisfactory agreement with the reference solutions of Karami et al. (2006) for all considered fiber orientation angles and boundary-stiffness parameters, with deviations remaining below approximately 6%.

Table 4. The first natural frequency parameter of a laminated plate with elastic boundary conditions

Method	θ	Boundary stiffness					
		10^1	10^2	10^3	10^4	10^6	10^8
Present	15^o	0.2020	0.5895	1.3189	1.8768	1.9924	1.9937
Karami et al. (2006)		0.2038	0.6066	1.3821	1.9416	2.0622	2.0635
Present	30^o	0.3413	0.9302	1.6468	1.8870	1.9209	1.9212
Karami et al. (2006)		0.3434	0.9618	1.7432	1.9971	2.0326	2.0330
Present	45^o	0.5785	1.3455	1.8140	1.8990	1.9093	1.9094
Karami et al. (2006)		0.5828	1.4064	1.9285	2.0173	2.0279	2.0280

To further verify the implementation of distributed elastic boundary conditions, the open cylindrical shell benchmark reported by Shi et al. (2016) is considered. The geometric parameters are $R = 2\,m, L = 1\,m, h = 0.05\,m$, and the opening angle is 28.6°. The material properties are $E = 210\,GPa, \nu = 0.3, \rho = 7800\,kg/m^3$. The dimensionless frequency parameter is defined as $\Omega = \omega L^2\sqrt{\frac{\rho h}{D_0}}$, where $D_0 = \frac{Eh^3}{12(1-\nu^2)}$. The distributed translational and rotational spring stiffnesses are normalized as $k_t = \overline{k}_t \frac{D_0}{L^3}$ and $k_r = \overline{k}_r \frac{D_0}{L}$, respectively, with physical units N/m^2 and N. Their contributions are integrated consistently along the supported element edges. Uniform meshes ranging from 8×8 to 32×32 elements are examined. As shown in Tables 5 and 6, the maximum differences from the reference FFFF and CCCC frequencies are 4.55% and 6.09%, respectively. When the normalized spring stiffness increases to 10^8, the predicted frequencies approach those obtained by directly imposing CCCC constraints, with differences below 0.002%. Furthermore, for intermediate normalized stiffness levels of 10^2 and 10^4, the maximum variation in the reported frequency parameters between the 24×24 and 32×32 meshes is approximately 0.43%. These results confirm the expected limiting behavior of the distributed elastic restraints and demonstrate satisfactory frequency convergence as the supported boundary edges are progressively refined together with the shell discretization.

Table 5. Comparison of the first four dimensionless frequency parameters of an open cylindrical shell under free and fully clamped boundary conditions, including the large-stiffness spring limit.

Boundary case	Source / solution	Mode 1	Mode 2	Mode 3	Mode 4
FFFF	Shi et al. (2016)	13.4800	21.1700	28.1300	34.4700
	Present SM-DSG4	12.8668	21.0694	27.8816	33.0341
	Difference (%)	−4.549	−0.475	−0.883	−4.166
CCCC	Shi et al. (2016)	46.1400	74.1100	79.1400	109.9500
	Present (direct constraints)	45.4063	71.0530	76.1344	103.2564
	Difference (%)	−1.590	−4.125	−3.798	−6.088
Large-stiffness limit	Present (spring = 1.0E+08)	45.4055	71.0527	76.1339	103.2557
	Difference from direct CCCC (%)	−0.001757	−0.000456	−0.000620	−0.000624

Table 6. Mesh-convergence study for the first two dimensionless frequency parameters at two intermediate normalized spring stiffness levels.

Mesh	Spring = 10^2 Mode 1	Spring = 10^2 Mode 2	Spring = 10^4 Mode 1	Spring = 10^4 Mode 2
8 × 8	18.1468	19.8640	42.0759	74.6999
12 × 12	18.0891	19.8607	41.3971	70.9100
16 × 16	18.0681	19.8596	41.1653	69.6760

Mesh	Spring = 10^2 Mode 1	Spring = 10^2 Mode 2	Spring = 10^4 Mode 1	Spring = 10^4 Mode 2
24 × 24	18.0520	19.8585	41.0013	68.8203
32 × 32	18.0457	19.8580	40.9441	68.5249

Finally, the transient implementation is validated through the linear response of a simply supported laminated spherical shell. The benchmark uses $a = b = 20$ in, $h = 2$ in, $R/a = 5$, and $a/h = 10$, with the unsymmetric cross-ply layup $[0°/90°]$. The orthotropic properties are $E_1 = 19.2 \times 10^6$ psi, $E_2 = 1.56 \times 10^6$ psi, $G_{12} = G_{13} = 0.82 \times 10^6$ psi, $G_{23} = 0.523 \times 10^6$ psi, $\nu_{12} = \nu_{21} = 0.24$, and $\rho = 0.00012$ lb·s²/in⁴. The transverse pressure is prescribed as $q(x, y, t) = q_0 \, sin(\pi x/a) \, sin(\pi y/b) \, F(t)$, with $q_0 = 2000$ psi, $t_p = 0.003$ s, and $\Delta t = 2.5 \times 10^{-6}$ s. The triangular and sinusoidal pulse histories are defined by Eqs. (72) and (73), respectively.

$$F_{tri}(t) = 1 - \frac{t}{t_p}, \quad 0 \le t \le t_p; \quad F_{tri}(t) = 0, \quad t > t_p. \tag{72}$$

$$F_{sin}(t) = \sin(\frac{\pi t}{t_p}), \quad 0 \le t \le t_p; \quad F_{sin}(t) = 0, \quad t > t_p. \tag{73}$$

The response is evaluated at the shell center using $w_0(t) = w(a/2, b/2, t)$ and $\hat{\sigma}_x(t) = \sigma_x(a/2, b/2, h/2, t)/q_0$. As shown in Fig. 7, the displacement and normalized stress histories predicted by the present formulation are in close agreement with the results of Kant and Kommineni (1994), confirming the accuracy of the transient implementation.

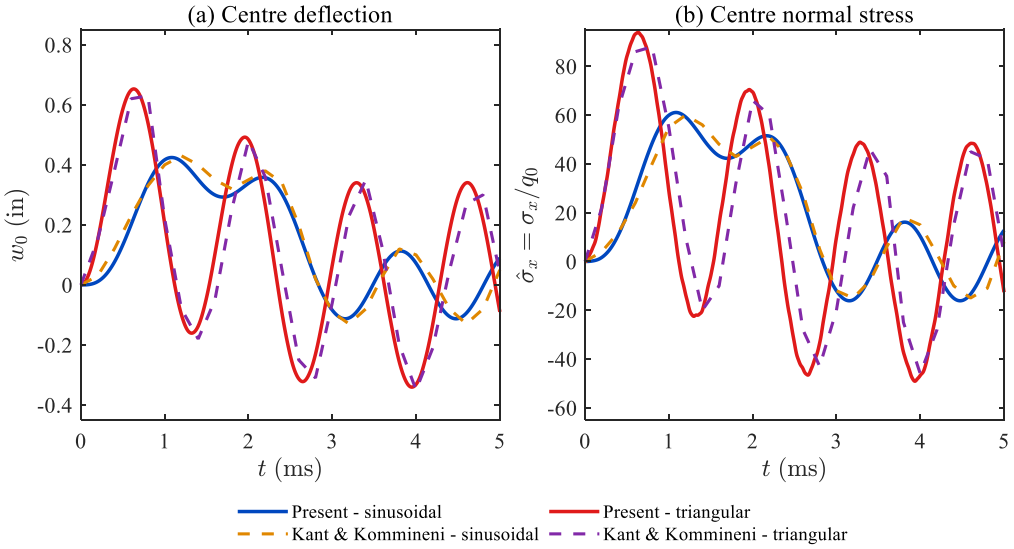


Figure 7. Transient response of a simply supported laminated spherical shell

4.2 Parametric results and physical discussion

4.2.1 Free-vibration analysis

Having established the accuracy of the present formulation, the material properties, layer configuration, thickness ratio, and auxetic honeycomb parameters used in the Table 2 benchmark are retained to investigate the first natural frequency f_1 of the sandwich shell under different curvature ratios and conventional boundary conditions. In the present analysis, the geometric ratio h/l is fixed at $h/l = 1$, while the curvature ratio is varied as $R/a = 5, 10, 100$. Four inclined angles of the auxetic unit cell, namely $\theta = -10°, -35°, -55°, -80°$, are considered. Seven conventional boundary conditions, including CCCC, CSCS, CCCF, SSSS, SCSF, CFCF, and CFFF, are examined. The first natural frequencies obtained from the proposed SM-DSG4 formulation are presented in Table 7. Here, C, S, and F denote clamped, simply supported, and free edges, respectively. It can be observed from Table 7 that the boundary condition has a pronounced effect on the first natural frequency of the sandwich shell. For all considered values of R/a and θ, the CCCC boundary condition gives the highest frequency, whereas the CFFF case produces the lowest value. This trend is physically reasonable because the fully clamped edges provide the strongest restraint and therefore increase the global stiffness of the structure, while the cantilever-type boundary allows larger deformation and consequently leads to lower

frequencies. The pronounced frequency reduction at a re-entrant angle of $-80°$ reflects changes in the equivalent elastic properties and mass density of the honeycomb core, which affect the membrane, bending, and transverse-shear stiffnesses relative to structural inertia. Furthermore, the decrease in natural frequency with increasing curvature ratio is consistent with the reduced contribution of curvature-induced membrane action as the shell becomes shallower.

Table 7. Dimensionless natural frequencies of honeycomb spherical shells with different boundary conditions

θ	R/a	Conventional boundary conditions						
		CCCC	CSCS	CCCF	SSSS	SCSF	CFCF	CFFF
-10	5	293.9509	236.6439	195.5363	171.4273	97.5277	184.8036	28.0324
-35		288.9292	233.6385	192.9754	168.9764	96.2527	182.4333	27.6610
-55		275.6219	222.9501	184.1468	161.0961	91.7811	174.0700	26.3680
-80		114.3475	92.7752	76.7181	66.1172	37.7910	72.4021	10.8094
-10	10	277.0552	223.7463	184.9193	156.9572	96.6431	173.3413	27.0215
-35		272.8863	220.9298	182.6036	154.8065	95.3847	171.1974	26.6774
-55		260.3770	210.8514	174.2741	147.5989	90.9530	163.3741	25.4301
-80		108.2227	87.9390	72.7588	60.6164	37.4439	68.1201	10.4196
-10	100	271.2352	219.3182	181.2361	151.8802	96.3257	169.3665	26.6694
-35		267.3685	216.5667	179.0059	149.8378	95.0732	167.3010	26.3352
-55		255.1346	206.6982	170.8501	142.8665	90.6559	159.6654	25.1038
-80		106.1198	86.2828	71.3893	58.6896	37.3194	66.6393	10.2842

The influence of boundary flexibility is further examined for a honeycomb sandwich spherical shell with elastic boundary conditions. The shell has the geometric parameters $a = b$, $h/l = 1$, and $a/h = 10$. Three curvature ratios are examined, namely $R/a = 5{,}10{,}100$, in order to clarify the effect of shell curvature. The auxetic honeycomb core is characterized by different inclined cell angles, $\theta = -10°, -35°, -55°, -80°$. The four edges of the shell are supported by distributed elastic springs, and the boundary stiffness is represented by the nondimensional parameter K, varying from 10^1 to 10^{10}. The first natural frequencies obtained by the proposed SM-DSG4 finite element formulation are listed in Table 8. It can be observed from Table 8 that the first natural frequency increases significantly as the elastic boundary stiffness K increases. This trend is physically reasonable because larger boundary stiffness reduces boundary flexibility and makes the shell behave closer to the corresponding simply supported limiting condition. For all curvature ratios and honeycomb angles, the frequency rises rapidly when K increases from 10^1 to 10^4, while it gradually converges when $K \geq 10^6$. The influence of shell curvature depends on the boundary restraint. Under highly flexible supports, the frequency variation with curvature is relatively small, whereas stronger edge restraint makes the effect of curvature-induced membrane action more pronounced. In addition, the honeycomb angle θ strongly affects the dynamic stiffness of the structure, and the lowest frequencies are generally obtained for $\theta = -80°$. Overall, Table 8 confirms that the proposed formulation can effectively capture the combined effects of elastic boundary conditions, shell curvature, and auxetic honeycomb geometry on the free-vibration behavior of sandwich spherical shells.

Table 8. Dimensionless natural frequencies of honeycomb spherical shells with elastic boundary conditions

h/l	a/h	θ	R/a	Boundary stiffness						
				10^1	10^2	10^3	10^4	10^6	10^8	10^{10}
1	10	-10	5	34.8076	108.7097	153.3299	165.0083	171.3218	171.4263	171.4273
		-35		34.1446	106.6486	150.9853	162.6204	168.8725	168.9754	168.9764
		-55		32.5298	101.6056	143.9392	155.0378	160.9971	161.0951	161.0961
		-80		13.2880	41.5055	59.1138	63.6458	66.0768	66.1168	66.1172

h/l	a/h	θ	R/a	Boundary stiffness						
				10^1	10^2	10^3	10^4	10^6	10^8	10^{10}
		-10	10	34.8338	108.8136	148.2841	154.8060	156.9241	156.9569	156.9572
		-35		34.1703	106.7502	146.1755	152.6746	154.7739	154.8062	154.8065
		-55		32.5543	101.7024	139.3640	145.5661	147.5678	147.5986	147.5989
		-80		13.2979	41.5448	57.2474	59.7848	60.6037	60.6163	60.6164
		-10	100	34.8422	108.8468	146.6236	151.4003	152.0296	152.0365	152.0365
		-35		34.1785	106.7827	144.5943	149.3565	149.9839	149.9907	149.9908
		-55		32.5621	101.7333	137.8600	142.4064	143.0056	143.0121	143.0122
		-80		13.3011	41.5573	56.6341	58.4980	58.7462	58.7489	58.7489

4.2.2 Transient analysis

The transient behavior of the honeycomb sandwich spherical shell is first examined under triangular, sinusoidal, and blast loads for conventional SSSS boundary conditions. The shell has side length $a = b = 20$ in, total thickness $h = 2$ in, and radius of curvature $R = 5a$. The sandwich thickness ratio of the bottom face sheet, honeycomb core, and top face sheet is $1: 1.5: 1$. The honeycomb angle is varied as $\theta = -10°, -35°, -55°, -80°$, while the remaining geometric, material, and numerical parameters are adopted from the preceding free-vibration studies. The time step and total analysis time are $\Delta t = 2.5 \times 10^{-6}$ s and $T = 0.005$ s, respectively. The center deflection w, center normal stress σ_x, center velocity $\dot{w}$, and phase diagram are used to characterize the transient response. For the triangular and sinusoidal pulses, the spatial distribution follows Eq. (33) with $q_0 = 2000$ psi, $t_p = 0.003$ s, and the time histories are given by Eqs. (72) and (73).

$$p_b(t) = P_0\left(1 - \frac{t}{t_p}\right) \exp\left(-\beta_b \frac{t}{t_p}\right), \quad 0 \le t \le t_p. \tag{74}$$

For the blast cases, Eq. (74) is used with $P_0 = 2000$ psi, $t_p = 0.003$ s, and $\beta_b = 1$, where P_0 is the peak pressure, t_p is the positive-phase duration, and β_b is the exponential decay parameter.

Figures 8 and 9 illustrate the transient responses of the auxetic honeycomb sandwich shell under triangular and sinusoidal pressure pulses, respectively. Under triangular loading, the center deflection, normalized normal stress, and velocity exhibit relatively regular oscillations, whereas the sinusoidal pulse produces a broader initial response peak and more complex phase-space trajectories. For re-entrant angles of $\theta = -10°, -35°$, and $-55°$, the responses exhibit comparable oscillation characteristics within each loading case. In contrast, the configuration with an angle of $\theta = -80°$ shows a noticeable change in the oscillation period and phase. This behavior is consistent with the free-vibration results, indicating that variations in the equivalent stiffness and inertia properties of the honeycomb core influence the transient response.

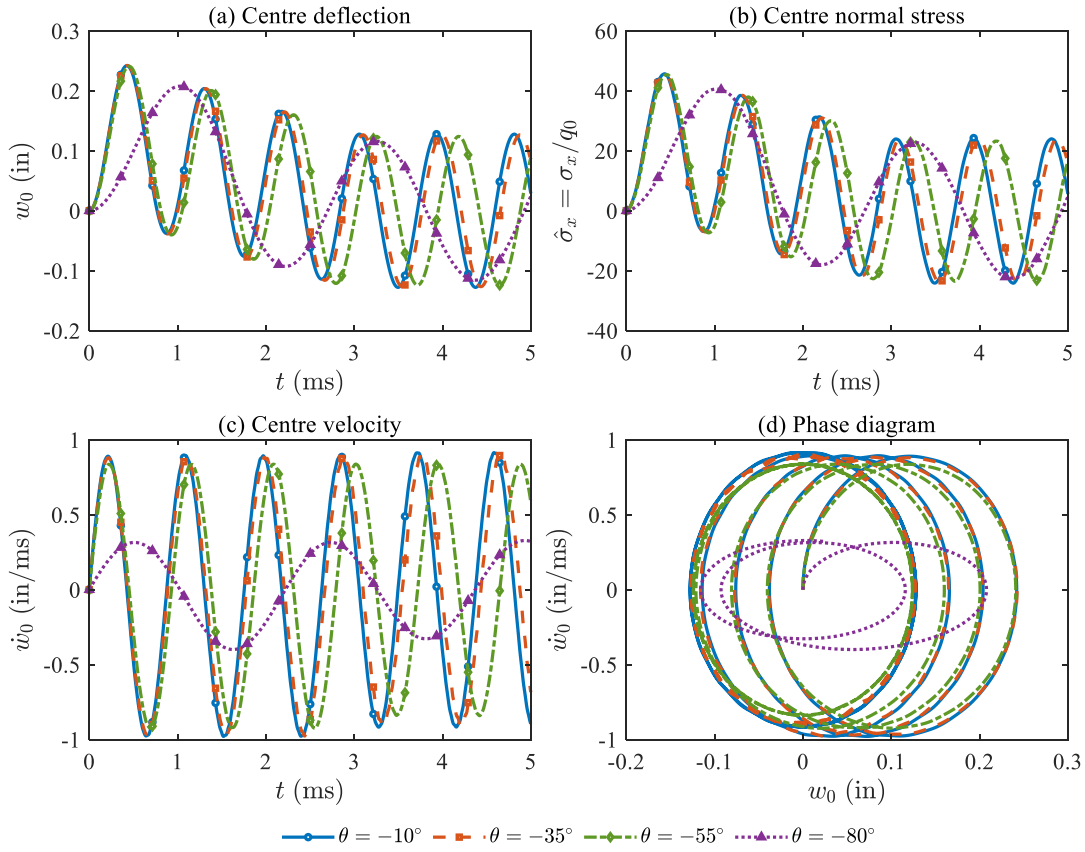


Figure 8. Transient response of SSSS honeycomb sandwich shells under triangular pulse loading

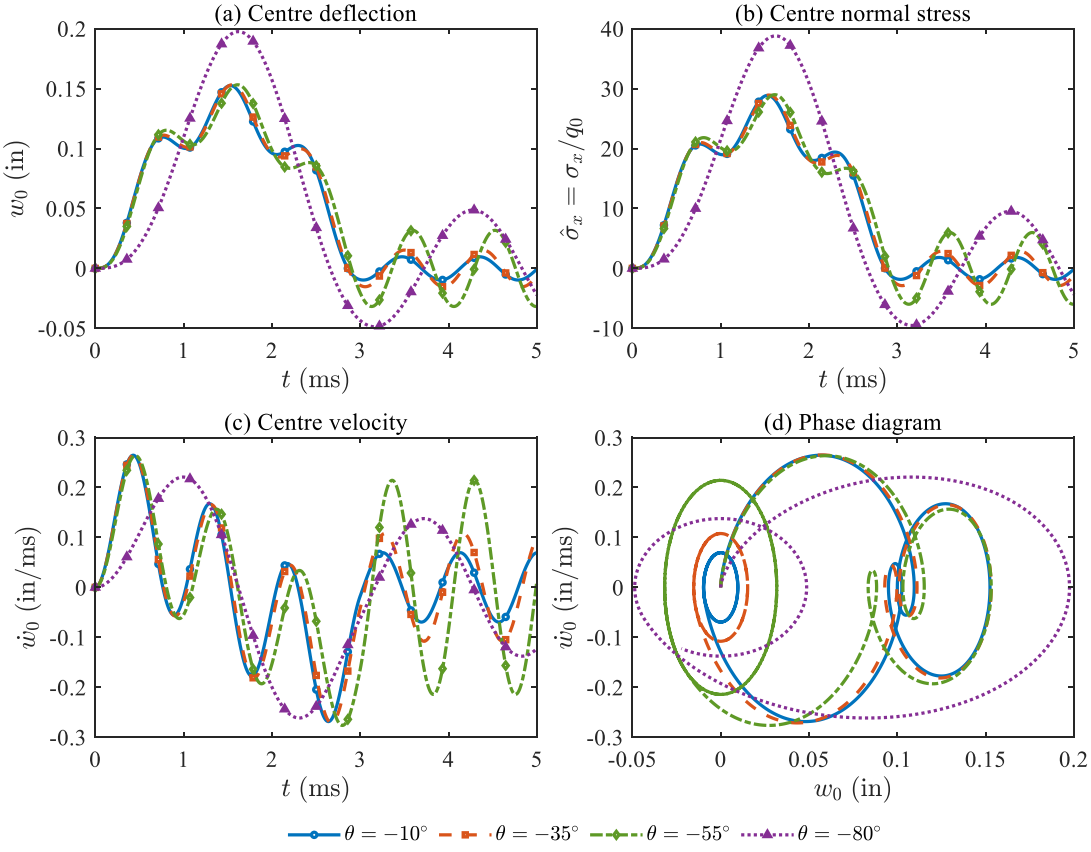


Figure 9. Transient response of SSSS honeycomb sandwich shells under sinusoidal pulse loading

Figure 10 shows the transient responses of the SSSS honeycomb sandwich shell under the prescribed blast-type pressure history. Although the triangular and blast-type pulses have the same peak pressure and positive-phase duration, the blast-type pressure decreases more rapidly owing to the exponential decay term. This difference in the temporal distribution of pressure can influence the excitation of the shell's vibration modes and its subsequent transient response.

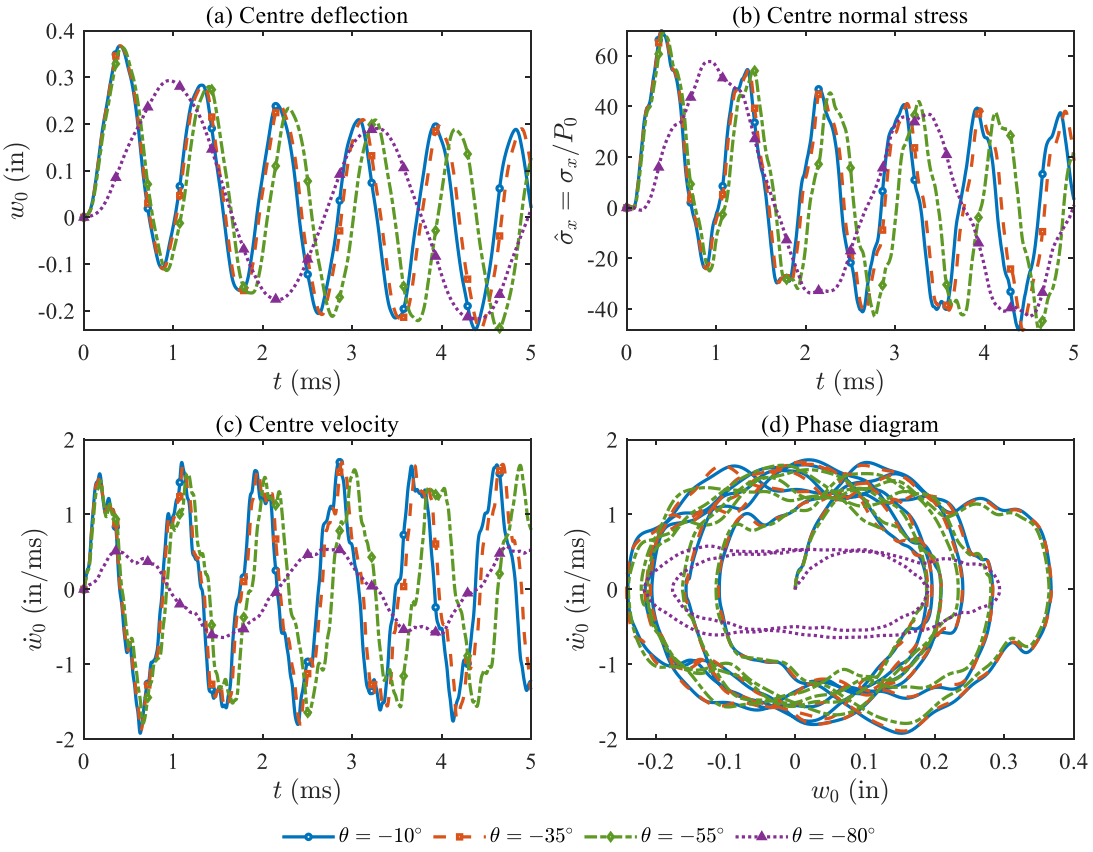


Figure 10. Transient response of SSSS honeycomb sandwich shells under blast loading

The analysis is then extended to honeycomb sandwich shells with SSSS-type elastic boundary conditions subjected to blast loading. Figures 11 and 12 summarize the corresponding responses. In the first case, the elastic boundary stiffness is fixed at $K = 10^2$, while different honeycomb angles $\theta = -10°, -35°, -55°$, and $-80°$ are considered. In the second case, the honeycomb angle is kept constant at $\theta = -35°$, whereas the elastic boundary stiffness varies from $K = 10^1$ to 10^4. The center deflection w_0, normalized center normal stress σ_x/P_0, center velocity $\dot{w}_0$, and phase diagram are used to evaluate the dynamic behavior of the shell. The results show that both the honeycomb angle and the elastic boundary stiffness have a significant effect on the blast-induced vibration response. Changing the honeycomb angle modifies the equivalent stiffness and inertia properties of the auxetic core, affecting the oscillation period, amplitude, and phase of the transient response. Increasing the boundary-spring stiffness restricts edge deformation and modifies the effective modal stiffness, leading to changes in the transient response amplitudes and phase trajectories. Therefore, the honeycomb geometric parameter and the elastic boundary condition should be carefully considered in the design of honeycomb sandwich shells subjected to blast loading.

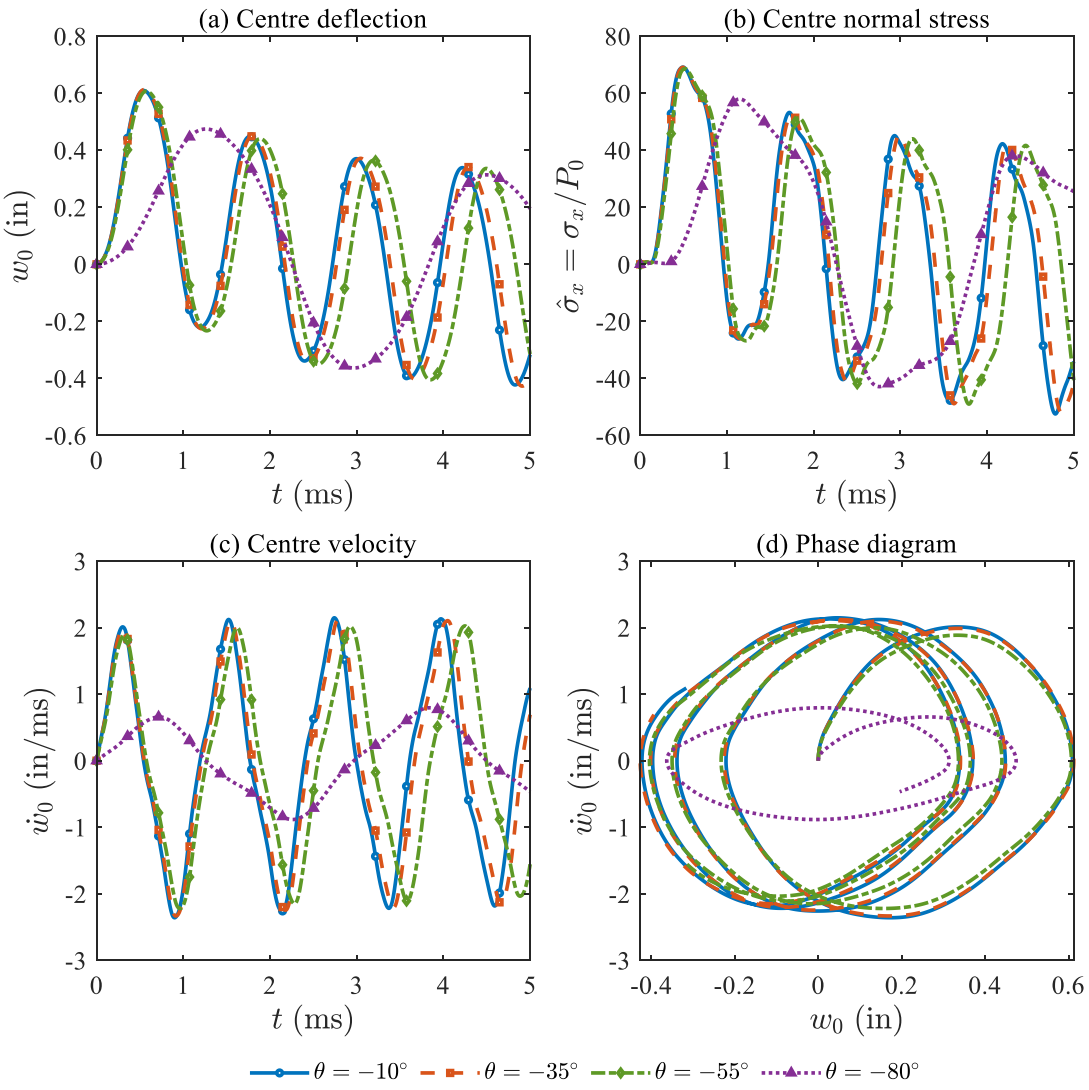


Figure 11. Blast response of honeycomb sandwich shells with SSSS-type elastic boundary conditions for different honeycomb angles ($K = 10^2$)

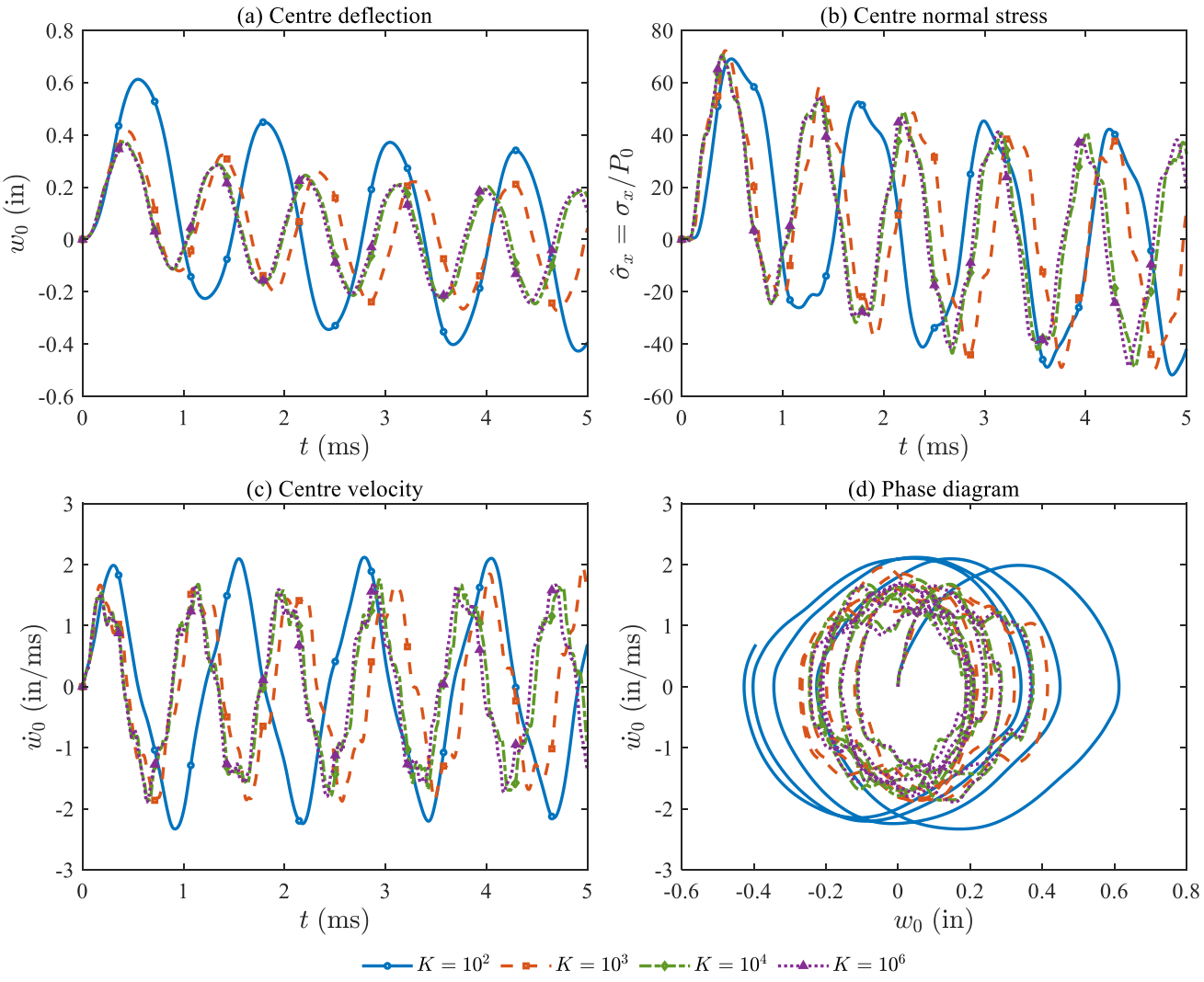


Figure 12. Blast response of honeycomb sandwich shells with SSSS-type elastic boundary conditions for different boundary stiffnesses ($\theta = -35^\circ$)

5 CONCLUSIONS

In this study, a cell-based smoothed DSG4 (SM-DSG4) flat-shell element was developed for the free-vibration and transient analyses of auxetic honeycomb sandwich shells with elastic boundary conditions. The re-entrant honeycomb core was represented by an equivalent orthotropic continuum, while distributed elastic springs were employed to account for boundary flexibility.

The numerical results demonstrate that the proposed SM-DSG4 element reduces the sensitivity of the fundamental frequency to mesh distortion compared with the conventional DSG4 element, with improvements of approximately 6.4–10.3% for the examined meshes at a distortion level of 0.3, without increasing the nodal degrees of freedom. The parametric analyses further reveal that shell curvature, re-entrant cell geometry, and boundary stiffness jointly influence the dynamic characteristics of sandwich shells. Curvature affects the structural response through membrane–bending coupling, while variations in the honeycomb cell angle modify the equivalent orthotropic properties of the core. Increasing the boundary stiffness restricts edge deformation, generally raises the natural frequencies, and changes the transient response characteristics.

These findings highlight the importance of accounting for both auxetic core geometry and support flexibility when predicting the dynamic behavior of sandwich shells. Nevertheless, the present formulation is limited to linear global structural responses based on a homogenized core model.

Conflicts of Interest: The authors declare that they have no competing interests.

Data availability: The data generated and analyzed during the current study are available from the corresponding author on reasonable request.

Editor: Marco L. Bittencourt

References

Abuteir, B.W., Boutagouga, D. (2022). Free-vibration response of functionally graded porous shell structures in thermal environments with temperature-dependent material properties. Acta Mech 233(11):4877–4901. https://doi.org/10.1007/s00707-022-03351-y

Bletzinger, K.U., Bischoff, M., Ramm, E. (2000). A unified approach for shear-locking-free triangular and rectangular shell finite elements. Comput Struct 75(3):321–334. https://doi.org/10.1016/S0045-7949(99)00140-6

Bohara, R.P., Linforth, S., Nguyen, T., Ghazlan, A., Ngo, T. (2022). Dual-mechanism auxetic-core protective sandwich structure under blast loading. Compos Struct 299:116088. https://doi.org/10.1016/j.compstruct.2022.116088

Burlayenko, V.N., Sadowski, T. (2020). Free vibrations and static analysis of functionally graded sandwich plates with three-dimensional finite elements. Meccanica 55:815–832. https://doi.org/10.1007/s11012-019-01001-7

Challamel, N., Wang, C.M., Reddy, J.N., Faghidian, S.A. (2025). Equivalence between micromorphic, nonlocal gradient, and two-phase nonlocal beam theories. Acta Mech 236(2):871–902. https://doi.org/10.1007/s00707-024-04180-x

Chen, G., Chen, L., Tang, J. (2022). An edge center based strain-smoothing element with discrete shear gap for the analysis of Reissner–Mindlin shell. Thin-Walled Struct 175:109140. https://doi.org/10.1016/j.tws.2022.109140

Cho, J.R. (2023). Free vibration analysis of functionally graded porous cylindrical panels reinforced with graphene platelets. Nanomaterials 13(9):1441. https://doi.org/10.3390/nano13091441

Cui, X., Liu, G.R., Li, G.Y., Zhang, G., Zheng, G. (2010). Analysis of plates and shells using an edge-based smoothed finite element method. Comput Mech 45:141–156. https://doi.org/10.1007/s00466-009-0429-9

Faghidian, S.A., Żur, K.K., Rabczuk, T. (2022). Mixture unified gradient theory: a consistent approach for mechanics of nanobars. Appl Phys A 128:996. https://doi.org/10.1007/s00339-022-06130-7

Faghidian, S.A., Elishakoff, I. (2023). A consistent approach to characterize random vibrations of nanobeams. Eng Anal Bound Elem 152:14–21. https://doi.org/10.1016/j.enganabound.2023.03.037

Faghidian, S.A., Darban, H. (2024). Non-standard interface conditions in flexure of mixture unified gradient nanobeams. Int J Eng Sci 204:104127. https://doi.org/10.1016/j.ijengsci.2024.104127

Farazin, A., Zhang, C., Abed, A.M. (2022). Vibrations of composite structures: finite element and analytical investigation. Polym Polym Compos 30. https://doi.org/10.1177/09673911221112956

Fu, T., Hu, X., Yang, C. (2023). Impact response analysis of stiffened sandwich functionally graded porous materials doubly-curved shell with re-entrant honeycomb auxetic core. Appl Math Model 124:553–575. https://doi.org/10.1016/j.apm.2023.08.024

Ghanbari, J., Panirani, P.N. (2024). A hybrid bio-inspired sandwich structures for high strain rate energy absorption applications. Sci Rep 14:2865. https://doi.org/10.1038/s41598-024-53521-2

Kant, T., Kommineni, J.R. (1994). Geometrically non-linear transient analysis of laminated composite and sandwich shells with a refined theory and C0 finite elements. Comput Struct 52(6):1243–1259. https://doi.org/10.1016/0045-7949(94)90188-0

Karami, G., Malekzadeh, P., Mohebpour, S.R. (2006). DQM free vibration analysis of moderately thick symmetric laminated plates with elastically restrained edges. Compos Struct 74(1):115–125. https://doi.org/10.1016/j.compstruct.2006.02.014

Kwak, S., Kim, K., Pang, K., Kim, S., Kim, P. (2022). Free vibration analysis of bulkhead-stiffened functionally graded open shell using a meshless method. Shock Vib 2022:7372167. https://doi.org/10.1155/2022/7372167

Lee, C., Lee, P.S. (2019). The strain-smoothed MITC3+ shell finite element. Comput Struct 223:106096. https://doi.org/10.1016/j.compstruc.2019.07.005

Li, H., Dong, B., Gao, Z., Zhao, J., Zhang, H., Wang, X., Han, Q. (2022). Analytical modeling and vibration analysis of fiber reinforced composite hexagon honeycomb sandwich cylindrical-spherical combined shells. Appl Math Mech 43(9):1307–1322. https://doi.org/10.1007/s10483-022-2858-7

Li, X., Peng, W., Wu, W., Xiong, J., Lu, Y. (2023). Auxetic mechanical metamaterials: from soft to stiff. Int J Extrem Manuf 5(4):042003. https://doi.org/10.1088/2631-7990/ace668

Li, Y., Yao, W., Wang, T. (2020). Free flexural vibration of thin-walled honeycomb sandwich cylindrical shells. Thin-Walled Struct 157:107032. https://doi.org/10.1016/j.tws.2020.107032

Li, Y.S., Liu, B.L. (2022). Thermal buckling and free vibration of viscoelastic functionally graded sandwich shells with tunable auxetic honeycomb core. Appl Math Model 108:685–700. https://doi.org/10.1016/j.apm.2022.04.019

Liguori, F.S., Zucco, G., Madeo, A. (2024). A geometrically nonlinear Hellinger–Reissner shell element for the postbuckling analysis of variable stiffness composite laminate structures. Meccanica 59:1351–1368. https://doi.org/10.1007/s11012-024-01799-x

Nguyen-Thanh, N., Rabczuk, T., Nguyen-Xuan, H., Bordas, S.P.A. (2008). A smoothed finite element method for shell analysis. Comput Methods Appl Mech Eng 198(2):165–177. https://doi.org/10.1016/j.cma.2008.05.029

Nguyen-Thoi, T., Phung-Van, P., Thai-Hoang, C., Nguyen-Xuan, H. (2013). A cell-based smoothed discrete shear gap method (CS-DSG3) using triangular elements for static and free vibration analyses of shell structures. Int J Mech Sci 74:32–45. https://doi.org/10.1016/j.ijmecsci.2013.04.005

Nguyen-Van, H., Mai-Duy, N., Tran-Cong, T. (2009). An improved quadrilateral flat element with drilling degrees of freedom for shell structural analysis. CMES-Comput Model Eng Sci 49(2):81–112. https://doi.org/10.3970/cmes.2009.049.081

Nguyen-Xuan, H., Liu, G.R., Thai-Hoang, C., Nguyen-Thoi, T. (2010). An edge-based smoothed finite element method (ES-FEM) with stabilized discrete shear gap technique for analysis of Reissner–Mindlin plates. Comput Methods Appl Mech Eng 199(9–12):471–489. https://doi.org/10.1016/j.cma.2009.09.001

Patel, M., Patel, S., Ahmad, S. (2023). Blast analysis of efficient honeycomb sandwich structures with CFRP/Steel FML skins. Int J Impact Eng 178:104609. https://doi.org/10.1016/j.ijimpeng.2023.104609

Pham, H.A., Tran, H.Q., Tran, M.T., Nguyen, V.L., Huong, Q.T. (2022). Free vibration analysis and optimization of doubly-curved stiffened sandwich shells with functionally graded skins and auxetic honeycomb core layer. Thin-Walled Struct 179:109571. https://doi.org/10.1016/j.tws.2022.109571

Pham, Q.H., Tran, T.V., Pham, T.D., Phan, D.H. (2018). An edge-based smoothed MITC3 (ES-MITC3) shell finite element in laminated composite shell structures analysis. Int J Comput Methods 15(7):1850060. https://doi.org/10.1142/S0219876218500603

Qing-Tian, D., Zhi-Chun, Y. (2010). Wave propagation in sandwich panel with auxetic core. J Solid Mech 2(4):393–402

Razgordanisharahi, A., Alipour Ghassabi, A., Hellmich, C. (2023). Free vibration analysis of cylindrical honeycomb sandwich panels using state-space Levy method. Thin-Walled Struct 182:110308. https://doi.org/10.1016/j.tws.2022.110308

Sayyad, A.S., Ghugal, Y.M. (2019). Static and free vibration analysis of laminated composite and sandwich spherical shells using a generalized higher-order shell theory. Compos Struct 219:129–146. https://doi.org/10.1016/j.compstruct.2019.03.054

Shi, D., Zhao, Y., Wang, Q., Teng, X., Pang, F. (2016). A unified spectro-geometric-Ritz method for vibration analysis of open and closed shells with arbitrary boundary conditions. Shock Vib 2016:4097123. https://doi.org/10.1155/2016/4097123

Siniauskaya, V., Wang, H., Liu, Y., Chen, Y., Zhuravkov, M., Lyu, Y. (2024). A review on the auxetic mechanical metamaterials and their applications in the field of applied engineering. Front Mater 11:1453905. https://doi.org/10.3389/fmats.2024.1453905

Thai-Hoang, C., Nguyen-Thanh, N., Nguyen-Xuan, H., Rabczuk, T., Bordas, S. (2011). A cell-based smoothed finite element method for free vibration and buckling analysis of shells. KSCE J Civ Eng 15(2):347–361. https://doi.org/10.1007/s12205-011-1092-1

Thang, P.T., Kim, C., Jang, H., Kim, T., Kim, J. (2025). Free vibration characteristics of honeycomb sandwich cylindrical shells reinforced with graphene nanoplatelets/polymer coatings. Aerosp Sci Technol 156:109744. https://doi.org/10.1016/j.ast.2024.109744

Tornabene, F., Viscoti, M., Dimitri, R. (2026). Electro-mechanical analysis of laminated anisotropic doubly-curved shells of arbitrary shape using higher-order theories. Meccanica 61:83. https://doi.org/10.1007/s11012-026-02143-1

Tran, T.T., Pham, Q.H., Nguyen-Thoi, T., Tran, T.V. (2020). Dynamic analysis of sandwich auxetic honeycomb plates subjected to moving oscillator load on elastic foundation. Adv Mater Sci Eng 2020:6309130. https://doi.org/10.1155/2020/6309130

Valencia Murillo, C.E., Gutierrez Rivera, M.E., Flores Samano, N., Celaya Garcia, L.D. (2023). A seven-parameter spectral/hp finite element model for the linear vibration analysis of functionally graded shells with nonuniform thickness. Appl Sci 13(20):11540. https://doi.org/10.3390/app132011540

Yin, F., Zhi, X., Fan, F., Wei, W., Zheng, D. (2023). Blast loads and variability on cylindrical shells under different charge orientations. Sci Rep 13:6719. https://doi.org/10.1038/s41598-023-30785-8